Linear Closed-Loop Control of Fluid Instabilities and Noise-Induced Perturbations: A Review of Approaches and Tools[1]

Denis Sipp
ONERA-The French Aerospace Lab,
Meudon F-92190, France
e-mail: denis.sipp@onera.fr

Peter J. Schmid
Department of Mathematics,
Imperial College London,
London SW7 2AZ, UK
e-mail: pjschmid@imperial.ac.uk

This review article is concerned with the design of linear reduced-order models and control laws for closed-loop control of instabilities in transitional flows. For oscillator flows, such as open-cavity flows, we suggest the use of optimal control techniques with Galerkin models based on unstable global modes and balanced modes. Particular attention has to be paid to stability–robustness properties of the control law. Specifically, we show that large delays and strong amplification between the control input and the estimation sensor may be detrimental both to performance and robustness. For amplifier flows, such as backward-facing step flow, the requirement to account for the upstream disturbance environment rules out Galerkin models. In this case, an upstream sensor is introduced to detect incoming perturbations, and identification methods are used to fit a model structure to available input–output data. Control laws, obtained by direct inversion of the input–output relations, are found to be robust when applied to the large-scale numerical simulation. All the concepts are presented in a step-by-step manner, and numerical codes are provided for the interested reader. [DOI: 10.1115/1.4033345]

1 Introduction

Closed-loop control of fluid flow is concerned with the targeted manipulation of inherent flow behavior to accomplish a prescribed objective [1–6]. It uses information from the flow (provided by sensors) to adapt to incoming perturbations and adjust to changing flow conditions. Closed-loop control is particularly devised for stabilizing hydrodynamic instabilities, such as Tollmien–Schlichting waves developing in boundary-layer flow or the vortex shedding mode in flow past a cylinder. It takes advantage of the strength of the intrinsic instability mechanisms of the system to manipulate the flow at minimal cost. In terms of applications, it allows us to diminish drag of transport vehicles (for example, by maintaining boundary layer flows in a laminar state), increase safety margins (for example, by promoting large-scale instabilities in the wake of transport aircraft to alleviate vortices), avoid structural fatigue (for example, by suppressing the Rossiter modes in open cavity flows), or suppress noise sources (for example, by mitigating the Kelvin–Helmholtz instabilities in jet flows).

Contrary to open-loop control, closed-loop control may in principle adjust to different operating conditions as it takes advantage of restricted knowledge of the current state through sensing of the flow. In this article, we focus on in-time (reactive) closed-loop control [7] which acts on the time-scales of the perturbations that are targeted: we therefore leave aside optimized open-loop control strategies (adaptive control), where measurements are solely used to modify the control law parameters in order to adjust to slowly varying operating conditions. Experimental implementations of in-time closed-loop control are scarce in literature. Most achievements deal with nearly parallel flows such as channel or boundary-layer flow [8–10], with open-cavity flows [11–17] or with bluff-body or backward-facing step flow [18–22]. This article focuses on model-based control, leaving aside model-free control-design techniques, such as manual phase-gain adjustments where the actuator signal is purely proportional to a measurement signal with a time-delay ($u(t) = Ky(t-\tau)$) [23–25], proportional-integral-derivative controllers [23,26], adaptive filters [9,13,15,27–29], and attempts to find an optimal compensator law by machine learning techniques [6,22].

An accurate model representing the flow dynamics from all the inputs (actuators and upstream disturbances) to all the outputs (sensors) is the corner-stone of the model-based in-time closed-loop control. In the following, we will review techniques to obtain linear (Sec. 1.1) and nonlinear models (Sec. 1.2). The design of a control law, which transforms the measurement signal into an actuator law, may be performed in many ways [30,31]. The primary design objective is performance—for example, minimizing the velocity fluctuations in some region of the flow field. However, performance is often not the sole objective under consideration, and it is sometimes more prudent to trade a reduction in performance for an increase in robustness. Robustness is understood as performance under a range of off-design conditions and uncertainty. A severe lack of robustness may degrade or even invalidate a control law. In the design process of a control law, in principle both performance and robustness should be targeted such that the resulting control law remains effective over a whole range of operating conditions. The principal model-based control design techniques that have been used in flow control are reviewed in Sec. 1.3. The objective and outline of this article then follow in Sec. 1.4.

1.1 Linear Models.

Linear models may be obtained either by discretization of the governing equations, by projection of these equations onto a given basis, or by directly identifying the dynamics between inputs (actuators) and outputs (sensors).

Discretizing the linearized Navier–Stokes equations straightforwardly yields state-space models, with a number of degrees-of-freedom proportional to the grid size. In two-dimensional configurations that exhibit nearly parallel flows, perturbations may be Fourier-transformed in the streamwise direction, which results in a low-dimensional 1D problem, where the state consists in the flow variables in the wall-normal direction [32–35]. For strongly nonparallel flows, the streamwise direction needs to be discretized: for example, in a synthetic wake governed by the Ginzburg–Landau equations (whose coefficients may be chosen to mimic cylinder flow [24,36]), a small-scale 1D model is obtained

[1]The FREEFEM++ and MATLAB codes published with this paper were current as of date of publication. Future updates of the codes associated with this paper will be available at https://github.com/denissipp/AMR_Sipp_Schmid_2016

Manuscript received September 20, 2015; final manuscript received March 13, 2016; published online May 3, 2016. Assoc. Editor: Jörg Schumacher.

with the state-variables distributed along the streamwise direction. If the full linearized Navier–Stokes equations are considered, very large models with states covering the entire 3D domain are obtained. One may take advantage of the physical mechanisms involved in the dynamics to simplify and reduce the dimension of the state. For example, steady streaks in pipe flow [37] may be described by parabolic approximations of the steady linear Navier–Stokes equations; this approach provides a linear model where time is replaced by the streamwise coordinate and where the state only involves the degrees-of-freedom at streamwise sections.

The above-mentioned models, which are based on a spatial discretization of the linearized Navier–Stokes equations, involve a large number of degrees-of-freedom, but not all are necessary for feedback control. For example, given an actuator and a sensor, states that are downstream of the sensor or upstream of the actuator are not necessary since they are not observable by the sensor or not controllable by the actuator. Model reduction methods have been introduced to drastically reduce the number of states and focus on the observable and controllable states or the most relevant states in the input–output transfer function.

Petrov–Galerkin projection methods of the linearized Navier–Stokes equations onto specific bases have so far been considered. For example, the most controllable modes (eigenvectors of the controllability Gramian) or the most observable and controllable modes (eigenvectors of the product of the controllability and observability Gramians, see Refs. [38–42]) provide models that preserve stability and lead, in the latter case, to approximations with an upper-bound error expressed in the $\mathcal{H}_\infty$ infinity-norm (this upper-bound is actually very conservative). If the flows are globally unstable, the stable subspace may be reduced using controllable/observable modes while the unstable subspace may explicitly be accounted for by direct/adjoint global modes [43,44]. Model reduction procedures based on the $\mathcal{H}_2$ -norm [45,46] have also been developed and are generally preferred because they yield a smaller size for the reduced-order models, since they only keep the most relevant energetic states. Once the basis has been determined, the subsequent projection step of the linearized Navier–Stokes equations onto the basis may be avoided by the use of identification methods, where the coefficients of a linear model from the inputs to the modes' coefficients may be obtained by fitting the model to available input–output data. For example, the eigensystem realization algorithm (ERA) [47,48] in the case where an impulse can be released from the input location or subspace identification methods [49,50] for the more general case may readily be used for this purpose.

Closed-loop control methods do actually not require that the state in the model represents physical structures, such as controllable/observable modes. Only the input–output dynamics from the actuator to the sensor is important. Considering solely actuator–sensor data, identification methods may again be used to determine the coefficients of the underlying linear model [51]. Different techniques are at hand. Wiener filters, which consider the input autocorrelations and the cross-correlation between inputs and outputs [8], require long records of input–output data in order to converge the second-order statistics. More efficient techniques consider raw input–output data in the time-domain. The ERA method [47] is advantageous in numerical studies [52,53] when a clean impulse can be released at the input location. For the more general case, autoregressive (AR)-exogeneous, autoregressive-moving-average-exogeneous (ARMAX), or AR-Markov linear models may be fitted to broadband input–output signals [54–56]. The observer-Kalman filter identification method (OKID, see Refs. [57,58]) is an optimized algorithm, requiring rather few data to converge and is robust to the presence of external noise. Alternatively, subspace identification methods may also be used and require in principle fewer parameters to tune [10,18,19,49,59]. In the case of an unstable dynamics, the system first needs to be stabilized (with an available controller) and the controller and observer dynamics may be identified with the observer-controller identification method [57,60,61]. Identification methods in the frequency domain have also been developed. For this, broadband input–output data may be Fourier-transformed or the input signal can be chosen as a monotone excitation [61]. The latter choice is of particular interest [62] since it enables us to account for weak nonlinearities by the describing functions methodology, which considers the amplitude of the response only at the forcing frequency, leaving aside the response on the harmonics [63]. High-order rational fits [61,62] or Loewner approximations [64] are then used to obtain the models.

In complex configurations, the physics of the particular flow under consideration may lead to simplified linear physical models. In the case of an open cavity flow [14,61,65,66], the full dynamics may, for example, be decomposed into different subcomponents, each one governed by simple analytical expressions.

Techniques allowing us to combine a series of linear models parameterized by an external control parameter (upstream velocity, angle of attack, etc.) into a single parameterized linear model are important in view of designing a closed-loop control law which is robust against variations in the considered parameters [67].

1.2 Nonlinear Models. Nonlinear state-space models may be obtained from the spatial discretization of the nonlinear Navier–Stokes equations. This leads to large-scale models, where the state involves degrees-of-freedom distributed over the entire spatial domain of interest [68–71] or over streamwise sections in the case of the parabolized Navier–Stokes equations [72].

A reduction of the size of these models may again be achieved by projecting the nonlinear Navier–Stokes equations onto a given basis. The most straightforward choice is the basis consisting of proper-orthogonal-decomposition (POD) modes [17,73–76], which replace the controllable modes (eigenvalues of the controllability Gramian) that have been introduced in the linear framework. Yet, the lack of an underlying mathematical foundation makes this undertaking more difficult, and models need to be stabilized (calibrated) due to the truncation of the POD basis [73,77–80]. Once the POD basis has been determined, the ill-conditioned projection step may be avoided by using identification methods: a transient set of velocity fields may be used to determine the unknown coefficients of the nonlinear model either by least-squares [81] or by more systematic direct-adjoint (4D-VAR) techniques [82]. A firmer mathematical framework for extracting nonlinear reduced-order models has recently appeared in the form of the POD-discrete-extrapolation-interpolation-method (DEIM) technique [83], which is based on additional POD bases for the representation of nonlinear terms. First applications to large-scale fluid problems are encouraging [84,85].

Nonlinear models capturing solely the dynamics between actuators and sensors (without progressing through the state variables) may also be obtained by fitting nonlinear-autoregressive exogeneous models to input–output data in the time-domain [86].

1.3 Control Design Techniques. Control design methods depend on the nature (linear or nonlinear) and size of the underlying fluid model (discretized Navier–Stokes equations or reduced-order models).

Model-based control design methods for small-scale systems are presented in standard textbooks [31,87]. Performance is commonly the primary objective that has been considered in fluid mechanics. In nearly parallel flows, both pole-placement techniques [32] and optimal $\mathcal{H}_2$-targeting the standard deviation of some sensor measurement have first been considered for models based on a discretization of the 1D linearized Navier–Stokes equations [1,33–35,88]. For more complex configurations, reduced-order models are first determined before pole-placement techniques [11], optimal $\mathcal{H}_2$-control [11,43,44,89,90], or system inversion [8,55,56] can be employed. Robust $\mathcal{H}_\infty$-control (closely related to noncooperative game theory) has previously been

applied to account for the non-normality of the linearized Navier–Stokes equations [1,33,91]. In the frequency domain, loop-shaping techniques may also be considered to tune performance by either optimizing the sensitivity transfer function (inverted M circles on a Nichols chart) [92] or by using $\mathcal{H}_\infty$-loop-shaping techniques [93] to target an objective loop transfer function; in fluid mechanics, such techniques have been used by several groups [12,25,53,62,94].

Accounting for uncertainty is a crucial point in model-based flow control. Reduced-order models are inherently approximate, and the effect of uncertainty on the stability and performance of the closed-loop system needs to be carefully assessed. To this end, determining gain and phase margins (PM) [90] or evaluating the infinity norm of sensitivity functions [53] are useful quantitative measures of stability robustness. Targeting both performance and stability robustness may be achieved with the loop-transfer-recovery (LTR) technique, which consists of artificially increasing actuator noise to render the estimation process faster. LTR has first been applied in flow control to account for Reynolds number variations [34,35]. Limitations of this technique have been pointed out and discussed quite early [95]: the existence of right-half plane zeros may limit the speed of the estimation process, so that one cannot decouple the dynamics of the observer from the dynamics of the controller. This was clearly observed in backward-facing step flow [90], where robustness margins are first improved as the fictitious noise is increased, before they deteriorate again for still higher noise levels.

Robust control design techniques have been introduced [96–99] to directly target robustness and therefore minimize the effect of model uncertainty or badly known coefficients. Considering the small-gain-theorem [97], it is found that stability robustness is directly related to the $\mathcal{H}_\infty$-norm of the closed-loop system between actuator noise and actuator signal (input-multiplicative (IM) perturbations). Minimizing this quantity therefore yields compensators that are maximally robust in terms of stability. Such techniques have been considered in experimental flow control studies [18,19]. In the frequency domain, loop-shaping techniques may be considered to also tune robustness by either optimizing the complementary sensitivity function (M circles on a Nichols chart) [12,53,92,94] or by using $\mathcal{H}_\infty$-loop-shaping techniques [25,93]. It has previously been acknowledged that nonlinearity can cause a lack of robustness [76]. Robust linear control design methods (although not specifically designed for that purpose) have been used to improve the robustness to finite-amplitude perturbations [36,88,100]. Along this line, various authors promote nonlinear control [76,101] as a key to overcoming this difficulty.

In large-scale systems, flow control can be viewed as an optimization problem and tackled by direct-adjoint techniques based on the full nonlinear Navier–Stokes equations [30]. It is not possible to implement a controller based on such methods in an experiment, due to the time it takes to perform the direct-adjoint iterations. Nonetheless, it is interesting to perform such control to understand what closed-loop control can achieve at best and also optimize a control setup (for example, where to optimally place actuators and/or sensors). Several studies have been undertaken along this line, based on either classical optimal control [37,69–72] or on more complex robust control (noncooperative game theory) [37,68,72,102–105].

1.4 Objective and Outline of This Article. From a physical point of view, we have to distinguish two flow categories according to their behavior as transition is approached [106]: oscillator flows, such as the flow past a cylinder at $\mathrm{Re} = 47 - 150$, are characterized by a well-defined peak in the frequency spectrum, which is rather insensitive to upstream perturbations; amplifier flows, on the other hand, such as a boundary-layer flow subject to Tollmien–Schlichting waves, exhibit a broadband frequency spectrum, which is a reflection of the upstream perturbation environment. Such distinct flow behaviors may straightforwardly be linked to distinct properties of the linear stability operator: oscillator flows are characterized by globally unstable operators with the frequency peak of the flow close to the frequency of the unstable global mode; amplifier flows correspond to globally stable operators with the non-normality of the operator [107] accounting for the potential of spatial amplification in the streamwise direction.

The distinction in behavior between oscillator and amplifier flows also causes difficulties of a different nature for building reduced-order models capturing all the inputs and outputs. In the case of oscillator flows, modeling the upstream disturbance environment poses less of an issue since the dynamics is rather independent of it. Models obtained by Galerkin projections are therefore well suited, and a combination of unstable global modes and balanced modes accounting solely for the actuator input [40,43,44] may be chosen as the projection basis. In the case of amplifier flows, where modeling the influence of upstream disturbances becomes crucial, Galerkin models are inappropriate due to their difficulty in obtaining an accurate representation of the upstream disturbance environment. A second approach is therefore introduced that identifies the input–output kernels [54,55] rather than deriving them from the governing equations. This approach is not model-free, since we still have to pose the structure of the input–output kernels. Yet, it relies less on an accurate description of the upstream disturbances: rather, the disturbance model is replaced or marginalized by processing information from an upstream sensor, which approximates the influence of upstream disturbances.

Note that the size of accurate reduced-order models is determined by both spatial and temporal features; both large delays between inputs and outputs and high-Reynolds number flows require an increased order of the models. In the presence of time delays, which is the case if the actuator and sensor are not co-located, the model order is generally governed by these time delays.

In this review, we introduce a framework for the design and assessment of control configurations. Two generic cases (oscillator and amplifier flows) will be considered, and the various concepts and techniques to build reduced-order models and to design controllers will be presented. Although the two cases seem different and appear to require different approaches, we will also observe a great deal of commonalities; most importantly, we will demonstrate the flexibility of the presented framework and make a particular effort at physical interpretations wherever possible. Special emphasis will be devoted to the robustness issue. Here, we consider the robustness of a control design as an a posteriori diagnostics; it is in turn used to motivate procedures to ameliorate robustness at a certain expense to performance. Nonetheless, an explicit promotion of robustness in the cost functional is beyond the scope of this review.

The outline of this article is as follows: After presenting the mathematical setup of the flow-control problem (Sec. 2), we successively deal with the case of oscillator flow (Sec. 3) and amplifier flow control (Sec. 4). A final section (Sec. 5) is devoted to an outlook of the field.

2 Mathematical Setup of the Flow Control Problem

The mathematical description of a flow control problem consists principally of the equations governing the motion of fluid flow under the influence of external forcing around which a compensator is designed that takes limited information from the flow field and feeds back a control strategy. The specifics of this control strategy are a central component of the design process and depend on the overall cost objective, but must in general also respect robustness and performance requirements.

Mathematically, we can state a system of equations in the form

$$\dot{\mathbf{x}} = \mathbf{f}(\mathbf{x}, u, w) \tag{1a}$$

$$y = \mathbf{f}_y(\mathbf{x}, g) \tag{1b}$$

$$z = \mathbf{f}_z(\mathbf{x}) \tag{1c}$$

The first equation (1*a*) represents an initial-value problem for the state vector $\mathbf{x}$, which fully describes the evolution of the fluid flow in time. This generally nonlinear equation also contains a control variable u, modeling the influence of outside forces on the flow development, as well as a noise term w accounting for commonly unknown sources of uncertainty and stochasticity, such as free-stream disturbances, acoustic noise source, and wall roughness distributions. Of course, the initial-value problem is also parameterized by governing parameters, in our case mainly by the Reynolds number Re. The second equation (1*b*) extracts information from the full flow field, usually with the help of a sensor or other measuring device. This measurement y is described by the (generally nonlinear) function $\mathbf{f}_y$ which contains both the sensor location and the type of signal (pressure, shear stress, temperature, etc.). An additional stochastic term g models measurement noise. The third equation (1*c*) resembles the second, as it also provides information about the full flow field $\mathbf{x}$ via the function $\mathbf{f}_z$. In the latter case, however, the signal z is not used to feed information about the flow to the compensator, rather it is used to define the control objective: once the compensator is attached to the system and the composite system is operating in closed-loop mode, the signal z is required to follow a prescribed behavior.

The three equations above are then supplemented by a compensator which establishes a link between the estimation measurement y and the control signal u such that a user-specified cost-objective (based on the second measurement, the performance measurement z) is reached. As is customary in flow control studies, a block diagram illustrates the interplay between fluid system and compensator in the closed-loop mode (see Fig. 1): the fluid system (referred to as *plant*) is driven by two inputs (the control signal u and external disturbances w) and produces two outputs (the measurement y and the cost objective signal z). The measurement y and control signal u are linked by a compensator whose task is to manipulate the closed-loop system such that the cost objective based on the performance signal z is optimally reached.

We focus in this article on the stabilization of equilibrium points $\mathbf{x}_0$ existing in transitional flows. These are defined as steady-state solutions of the governing equations

$$\mathbf{f}(\mathbf{x}_0, u = 0, w = 0) = 0 \tag{2}$$

The control objectives in this article are concerned with the maintenance of the flow near some equilibrium point which involves the suppression of instabilities (in the globally unstable case) or the reduction of perturbation variance (in the globally stable case). Mathematically, the focus on flow in the neighborhood of an equilibrium point allows the linearization of the governing equations. In addition, we will assume a discretization of the spatial coordinates introducing matrices in lieu of linear operators and state vectors in lieu of state variables. We obtain

$$\dot{\mathbf{x}} = \mathsf{A}\mathbf{x} + \mathsf{B}_u u + \mathsf{B}_w w \tag{3a}$$

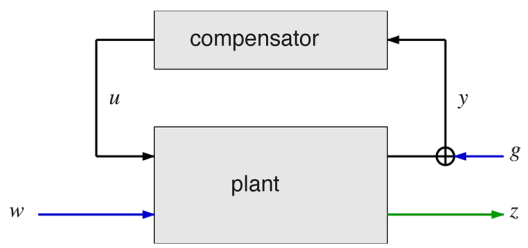

Fig. 1 Block diagram of a typical feedback control setup, including plant, compensator, external disturbance sources (w, g), control signal u, measurement signal y, and objective output z

$$y = \mathsf{C}_y\mathbf{x} + g \tag{3b}$$

$$z = \mathsf{C}_z\mathbf{x} \tag{3c}$$

where the system matrix A is given as $\mathsf{A} = \partial\mathbf{f}/\partial\mathbf{x}|_{\mathbf{x}_0}$ and analogously for the control matrix B_u, the measurement matrix C_y, and the objective matrix C_z. We assume the disturbance source w and sensor noise g to carry over as additive sources of random noise, which is in general the case when both w and g display weak amplitudes. The matrix B_w models the manner in which plant noise w forces the plant. In a slight abuse of notation, $\mathbf{x}$, y, and z in these equations in fact correspond, respectively, to the perturbed quantities $\mathbf{x} - \mathbf{x}_0$, $y - y_0$, and $z - z_0$.

The sketch of the closed-loop system (Fig. 1) suggests the importance and advantage of an input–output description of a linear system. This is accomplished by defining a transfer function, a concept that will be utilized in model reduction and system identification of linear open-loop systems and design and performance analysis of closed-loop systems. The transfer functions are derived from Eqs. (3*a*) to (3*c*) via Laplace transforms. For example, the transfer function T_{yu} from the input signal u to the output measurement y for the (linearized) plant is given as

$$\mathsf{T}_{yu}(s) = \mathsf{C}_y(s\mathsf{I} - \mathsf{A})^{-1}\mathsf{B}_u \tag{4}$$

with s as the Laplace variable. For purely imaginary arguments $s = i\omega$, it describes the relative amplification or suppression of harmonic input signals (of frequency ω) as they pass through the linear system. The transfer function can thus be interpreted as the filter function of the linear plant. The transfer function T_{yu} from the input signal u to the estimation measurement y characterizes the strength of the feedback and will be particularly important for robustness issues. The transfer functions T_{zu} and T_{zw} involving the performance signal z are important for performance and T_{yw} for detection of upstream disturbances.

Before proceeding with the definition and design of closed-loop flow control problems, we need to analyze the dynamics of the flow to be manipulated, in order to identify the key mechanism which drives the unsteadiness. This crucially depends on the stability behavior of the unforced (uncontrolled) system. Two cases can be distinguished: (i) fluid flows that are globally unstable and are thus dominated by an oscillatory instability and (ii) fluid flows that are globally stable [106]. Fluid systems of the former case, referred to as *oscillators*, are rather insensitive to external noise sources, whereas fluid systems of the latter case, known as *amplifiers*, react sensitively and distinctly to exogenous stochastic disturbances. Our control objective for oscillator flows is the suppression of the inherent instabilities, while for amplifier flows it is the reduction of noise amplification (measured, e.g., by the signal variance) throughout the system. The design steps for each type of system are rather distinct, and this article is presenting the principal steps for the effective and robust control design for either case. We will showcase the control design and performance evaluation on two generic flow configurations: the flow over an open cavity, which for sufficiently large Reynolds number acts as an oscillator [108], and the flow over a backward-facing step, which falls into the noise-amplifier category [109]. The two configurations are sketched in Fig. 2, together with the actuator/sensor setup which will be discussed in more detail below. We thus proceed with designing a flow control strategy for flow over an open cavity, outlining the procedural steps while paying particular attention to questions of performance, closed-loop stability, and robustness.

3 Control of Oscillators: Flow Over an Open Square Cavity

The open-square cavity configuration is fully described in Sipp and Lebedev [108]. We use the mesh referenced D1 and the

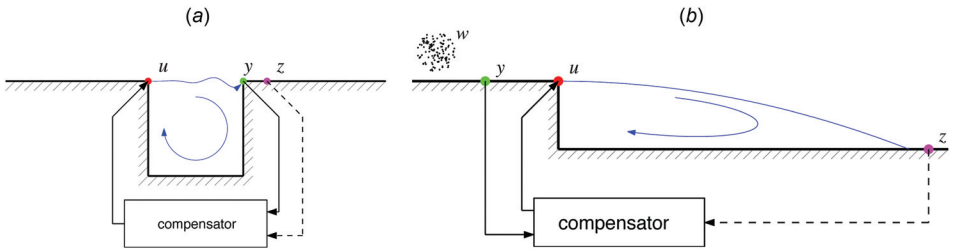

Fig. 2 Sketch of flow over an open cavity (*a*) and a backward-facing step (*b*)—two generic flow configurations representing an oscillator and noise-amplifier flow, respectively. The actuator (*u*), flow sensor (*y*), and performance sensor (*z*) are marked by colored symbols for each configuration. External upstream disturbance sources are indicated by *w* in the case of an amplifier flow. (*a*) Feedback configuration and (*b*) feed-forward configuration.

identical boundary conditions. The configuration is sketched in Fig. 2(*a*), with the flow entering the domain from the left. The boundary layer developing on the lower wall detaches at the left edge of the cavity and forms a shear layer, which separates the recirculation motion inside the cavity from the external flow. All the quantities are nondimensionalized by the cavity length and the upstream velocity; the Reynolds number is based on these same quantities. The actuator consists of a volume forcing, added to the cross-stream velocity equation and located near the upstream edge, while the sensor extracts shear-stress information close to the downstream edge. The exact actuator and sensor definitions are given in Barbagallo et al. [110].

The flow becomes globally unstable once a critical Reynolds number of $\mathrm{Re}_c = 4140$ is surpassed [108]; beyond this Reynolds number (based on the inflow freestream velocity and cavity depth), the flow acts as an oscillator, as the shear layer spanning the cavity exhibits instabilities due to pressure feedback between the downstream and upstream cavity edge. We will consider the flow at four supercritical Reynolds numbers, $\mathrm{Re} = 5250$, 6000, 7000, and 7500. A global stability analysis shows two (for $\mathrm{Re} = 5250$), three (for $\mathrm{Re} = 6000$ and 7000), or four (for $\mathrm{Re} = 7500$) eigenvalues, together with their symmetric counterparts. The eigenvalues, for positive frequencies, are displayed in Fig. 3(*a*). The least stable global mode for $\mathrm{Re} = 7500$ is shown in Fig. 3(*b*), visualized by the streamwise velocity component. The instability of the shear layer spanning the open cavity is clearly visible, together with a characteristic wavelength in the streamwise direction and a monotonic growth between the upstream and downstream cavity edge. The corresponding adjoint global mode, i.e., the principal global mode of the adjoint problem based on the conjugate transpose system matrix A^*, is shown in Fig. 3(*c*). This adjoint mode contains sensitivity information for the associated direct mode; not surprisingly, the adjoint mode is spatially compact near the upstream cavity edge, since this area displays the maximum sensitivity for exciting the corresponding direct global mode.

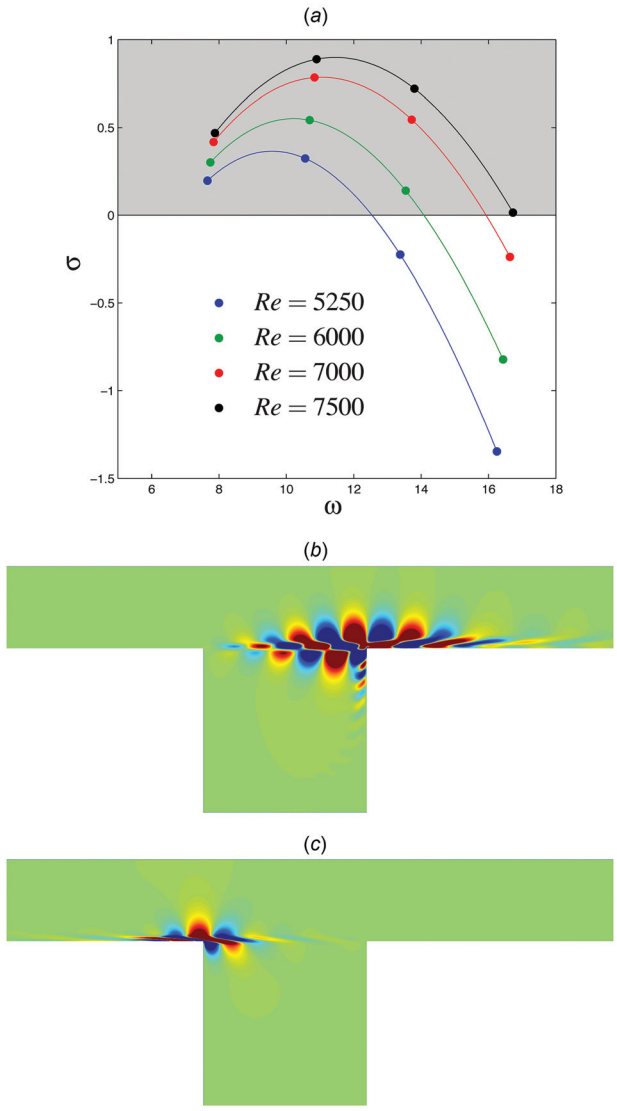

Fig. 3 (*a*) Eigenvalues for flow over an open cavity for four different Reynolds numbers, displayed in the complex frequency (ω)–growth-rate (σ) plane. (*b*) Principal global modes for flow over an open square cavity at $\mathrm{Re} = 7500$, visualized by contours of streamwise velocity. (*c*) Corresponding adjoint global mode.

Setting up the configuration [108]*?*
Linux commands (all codes are provided as Supplemental material, which is available under the "Supplemental Data" tab on the ASME Digital Collection):

1. cd Cavity/BF
2. FreeFem++ newton.edp # compute base-flow
3. cd ../Actuator
4. FreeFem++ actuator.edp # generate volume force representing actuator
5. cd ../Sensor
6. FreeFem++ sensor.edp # generate vector representing sensor

Comments. The base-flow $\mathbf{x}_0$ is a steady solution of the incompressible Navier–Stokes equations:

$$\mathbf{f}(\mathbf{x}_0) = \begin{pmatrix} -\mathbf{u}_0 \cdot \nabla \mathbf{u}_0 - \nabla \mathsf{p}_0 + \nu \Delta \mathbf{u}_0 \\ \nabla \cdot \mathbf{u}_0 \end{pmatrix} \tag{5}$$

where $(\mathbf{u}_0, \mathsf{p}_0)$ designate the velocity and pressure components of the base flow. We use finite-elements to spatially discretize these equations (FreeFem++). The discretization is first-order, if Arnold–Brezzi–Fortin MINI elements [111] are used or second-order with Taylor-Hood elements.

A Newton method may be used to find zeros of this nonlinear equation (code Cavity/BF/newton.edp). We therefore iteratively solve the equation

$$\delta\mathbf{x}_0 = -\mathsf{A}^{-1}[\mathbf{f}(\mathbf{x}_0)] \tag{6}$$

and set $\mathbf{x}_0^{\text{new}} = \mathbf{x}_0 + \delta\mathbf{x}_0$. The matrix A acts on the velocity–pressure components $\delta\mathbf{x} = (\delta\mathbf{u}, \delta\mathsf{p})^*$ of a perturbation around the current base flow $\mathbf{x}_0 = (\mathbf{u}_0, \mathsf{p}_0)$. It is obtained by spatially discretizing the linearized Navier–Stokes operator around $(\mathbf{u}_0, \mathsf{p}_0)$

$$\mathsf{A} = \begin{pmatrix} -() \cdot \nabla\mathbf{u}_0 - \mathbf{u}_0 \cdot \nabla() + \nu\Delta() & -\nabla() \\ \nabla \cdot () & 0 \end{pmatrix} \tag{7}$$

The inverse in Eq. (6) may be computed using a sparse, direct LU solver (e.g., MUMPS [112]).

How to determine unstable direct and adjoint eigenvalues [108]?
Linux commands:

1. cd ../Eigs
2. FreeFem++-nw eigen.edp # Compute unstable direct global modes
3. FreeFem++-nw eigenadj.edp # Compute unstable adjoint global modes
4. FreeFem++ plotUvvpc.edp # plot least-damped adjoint global mode

Comments. In order to determine the eigenvalues of A close to a given complex shift s, we compute the eigenvalues with largest magnitude of $(\mathsf{A} - s\mathsf{I})^{-1}$. For this, we repeatedly apply this operator to a given vector (power method), where the inverse operations are again carried out by a direct solver. Convergence may be improved by using a Krylov subspace and restarting techniques (e.g., Arnoldi methods [113]). The direct operator A (code Cavity/Eigs/eigen.edp) has been defined in Eq. (7), while the operator A^* can be obtained either by a conjugate transpose of A (code Cavity/Eigs/eigenadj.edp) or by discretization of the continuous adjoint operator

$$\mathsf{A}^* = \begin{pmatrix} -() \cdot \nabla\mathbf{u}_0^* + \mathbf{u}_0 \cdot \nabla() + \nu\Delta() & \nabla() \\ \nabla \cdot () & 0 \end{pmatrix} \tag{8}$$

How to perform a direct numerical simulation (DNS) of the incompressible Navier–Stokes equations?
Linux commands:

1. cd ../DNS
2. FreeFem++-nw init.edp # generate initial condition
3. FreeFem++-nw dns.edp # launch DNS solver

Comments. After spatial discretization, the Navier–Stokes equations may be written in the following perturbation form:

$$\frac{d\mathbf{u}}{dt} + \mathbf{u} \cdot \nabla\mathbf{u}_0 + \mathbf{u}_0 \cdot \nabla\mathbf{u} + \nabla\mathsf{p} - \nu\Delta\mathbf{u} = -\mathbf{u} \cdot \nabla\mathbf{u} \tag{9a}$$

$$\nabla \cdot \mathbf{u} = 0 \tag{9b}$$

where $(\mathbf{u}, \mathsf{p})$ denote the velocity and pressure components of a perturbation around the base flow $\mathbf{x}_0$. These equations may be time-discretized using a second-order semi implicit backward-finite-difference scheme. In the case of weak-amplitude perturbations (term $\mathbf{u} \cdot \nabla\mathbf{u}$ is weak), the code is unconditionally stable. Here, we reproduce (for simplicity) the first-order scheme

$$\begin{pmatrix} \frac{1}{\Delta t} + () \cdot \nabla\mathbf{u}_0 + \mathbf{u}_0 \cdot \nabla() - \nu\Delta() & \nabla() \\ \nabla \cdot () & 0 \end{pmatrix} \begin{pmatrix} \mathbf{u}^{n+1} \\ \mathsf{p}^{n+1} \end{pmatrix} = \begin{pmatrix} \frac{\mathbf{u}^n}{\Delta t} - \mathbf{u}^n \cdot \nabla\mathbf{u}^n \\ 0 \end{pmatrix} \tag{10}$$

This results in a large-scale linear system for $(\mathbf{u}^{n+1}\mathsf{p}^{n+1})^*$, which has to be inverted at each time-step (code Cavity/DNS/dns.edp). Supplemental material is available under the "Supplemental Data" tab on the ASME Digital Collection. The inversion is again performed using the direct LU-solver. Note that Dirichlet-boundary conditions can straightforwardly be enforced at this stage.

3.1 Model Reduction for Unstable Systems. Standard techniques of control design for the closed-loop setup shown in Fig. 1 result in a compensator that contains as many degrees-of-freedom as contained in the plant. This is a consequence of the estimator component (Kalman filter) of the compensator which reconstructs an approximate state vector from the measurements y supplied by the plant. A controller then uses this estimated state to determine the optimal control strategy u. It should be self-evident that for a control signal to be effective, it has to be available to the plant before the fluid system evolves over the next time step; in other words, the compensator has to react to changes in measurements on a faster time-scale than the characteristic time-scale of the plant. For a real-time capability of the compensator in experiments, it has to operate with few degrees-of-freedom. The strategy is then to reduce the plant from a high-dimensional system to an equivalent low-dimensional system, followed by the standard design of a reduced-order compensator based on the low-dimensional system. The term "equivalent" needs to be further specified: referring back to Fig. 1, it appears critical to match the input–output relations (or transfer functions) of the full and reduced system during the model-reduction process. In the present case-study, the high-dimensional transfer-function T_{yu} has been represented in Fig. 4 by a solid black line. We now attempt to find a reduced-order model, indicated by an over-bar $\overline{(\cdot)}$, with transfer functions, e.g., $\overline{\mathsf{T}}_{yu}$, that are close to the respective transfer functions of the full system, e.g., T_{yu}, where closeness is measured in the infinity-norm.

Technically, the model reduction process can be described by a Galerkin projection, where we express the state vector $\mathbf{x} \in \mathbb{R}^N$ in a given basis $\mathsf{V} \in \mathbb{C}^{N\times k}$ according to $\mathbf{x} \approx \mathsf{V}\overline{\mathbf{x}}$, where $\overline{\mathbf{x}} \in \mathbb{C}^k$ denotes the expansion coefficients. It is understood that $k \ll N$. To complete the projection, a second basis $\mathsf{W} \in \mathbb{C}^{N\times k}$ is necessary which is bi-orthogonal to V, such that $\mathsf{W}^*\mathsf{V} = \mathsf{I}$ with $\mathsf{I} \in \mathbb{C}^{k\times k}$ as the identity matrix. A system with k degrees-of-freedom for the coefficient vector $\overline{\mathbf{x}}$ can then be derived, resulting in

$$\dot{\overline{\mathbf{x}}} = \overline{\mathsf{A}}\overline{\mathbf{x}} + \overline{\mathsf{B}}_u u + \overline{\mathsf{B}}_w w \tag{11a}$$

$$y = \overline{\mathsf{C}}_y\overline{\mathbf{x}} + g \tag{11b}$$

$$z = \overline{\mathsf{C}}_z\overline{\mathbf{x}} \tag{11c}$$

with $\overline{\mathsf{A}} = \mathsf{W}^*\mathsf{A}\mathsf{V}$ as the reduced system matrix, and similarly expressions for $\overline{\mathsf{B}}_u$, $\overline{\mathsf{B}}_w$, $\overline{\mathsf{C}}_y$, and $\overline{\mathsf{C}}_z$. What remains to be determined is the basis V. The perturbation dynamics for flow over a

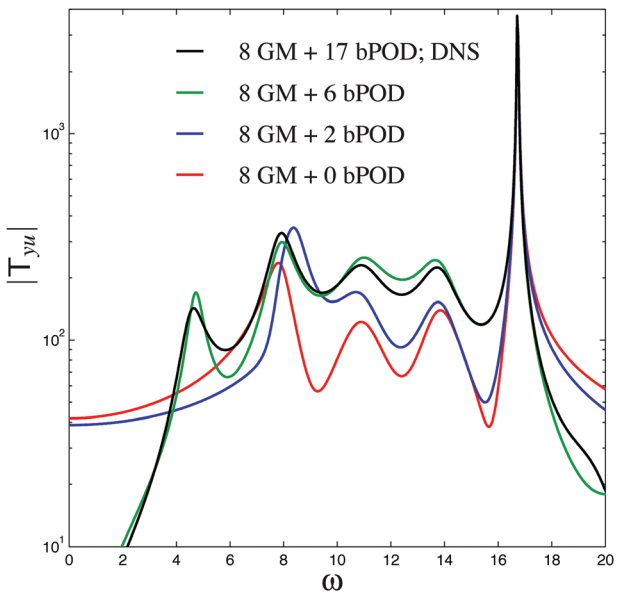

Fig. 4 Modulus of transfer functions for different compositions of the Galerkin bases for flow over an open cavity at Re = 7500. The bases are composed of eight global modes (8 GM) and a varying number of balanced (bPOD) modes.

cavity at supercritical Reynolds numbers ($\mathrm{Re} > 4140$) evolves in an unstable and stable subspace. Both subspaces have to be properly represented during the model-reduction process or the Galerkin projection. V and W are therefore compound of an unstable (V_u and W_u) part and a stable (V_s and W_s) part. For the unstable subspace, we choose the unstable direct and adjoint global modes for our expansion basis $(\mathsf{V}_u, \mathsf{W}_u)$. For the stable subspace, we refer back to the previous statement that the input–output dynamics $(u, w) \rightarrow (y, z)$ have to be captured by the selected basis vectors. For this reason, we choose a set of balanced modes for $(\mathsf{V}_s, \mathsf{W}_s)$. Balanced modes are characterized by structures that are equally observable and controllable and are thus particularly apt at spanning the dynamics between actuator and sensors. The balanced modes can be easily computed by a snapshot-based technique introduced by Willcox and Peraire [39] and Rowley [40]. Since this technique relies on a stable system, the snapshots have to be projected onto the stable subspace. This can be easily accomplished using the adjoint global modes corresponding to unstable modes.

Due to the presence of global instabilities, which dominate the fluid behavior, we choose a simple configuration with no external disturbance influences. However, we do include two uncorrelated sources of noise: the measurement noise g and the noise introduced into the system together with the control signal u (from which it follows that $\overline{\mathsf{B}}_w = \overline{\mathsf{B}}_u$). These noise sources are related to our output and input devices. We will denote the latter noise source by w and adjust the earlier block diagram according to Fig. 5. The principal balanced mode between $u = w$ and $y = z$ (we have chosen $\overline{\mathsf{B}}_w = \overline{\mathsf{B}}_u$ and $\overline{\mathsf{C}}_z = \overline{\mathsf{C}}_y$) and its adjoint are displayed in Fig. 6; they show a representation of the perturbation dynamics between the actuator and sensor. The composite model-reduction step for an unstable fluid system is sketched in Fig. 7. The bases contain unstable global modes (in red) in V_u and their adjoints in W_u, augmented by balanced modes (in green) in V_s and their adjoints in W_s. The Galerkin projection yields a substantially reduced system matrix $\overline{\mathsf{A}}$: the unstable part consists of a diagonal submatrix containing the unstable eigenvalues, the stable part is a dense submatrix of small dimension. The transfer functions associated with this reduced-order system may be obtained straightforwardly, e.g.,

$$\overline{\mathsf{T}}_{yu}(s) = \overline{\mathsf{C}}_y (s\overline{\mathsf{I}} - \overline{\mathsf{A}})^{-1} \overline{\mathsf{B}}_u \tag{12}$$

In order to validate the model-reduction process, we determine the transfer functions for different dimensionalities k of the Galerkin bases V and W. For a Reynolds number of $\mathrm{Re} = 7500$, the bases consist of eight unstable global modes (four complex conjugate pairs) augmented by a varying number of balanced modes (bPOD modes), see Fig. 4. The representation of only the unstable subspace (8 GM + 0 bPOD) captures the largest peak of the full transfer function, but fails to match at other frequencies. For increasing numbers of included balanced modes, the transfer function of the reduced system rapidly converges toward the transfer function of the full system. Once 17 balanced modes have been incorporated into V and W, the transfer functions of the full and reduced system are indistinguishable within plotting accuracy. In this latter case, the 25-dimensional system accurately reproduces the input–output behavior of the full high-dimensional system.

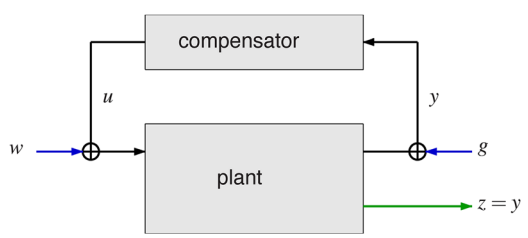

Fig. 5 Block diagram of a typical feedback control setup for oscillator flows, including plant, compensator, external noise sources $(\boldsymbol{w}, \boldsymbol{g})$, control signal $\boldsymbol{u}$, measurement signal $\boldsymbol{y}$, and objective output $\boldsymbol{z}$

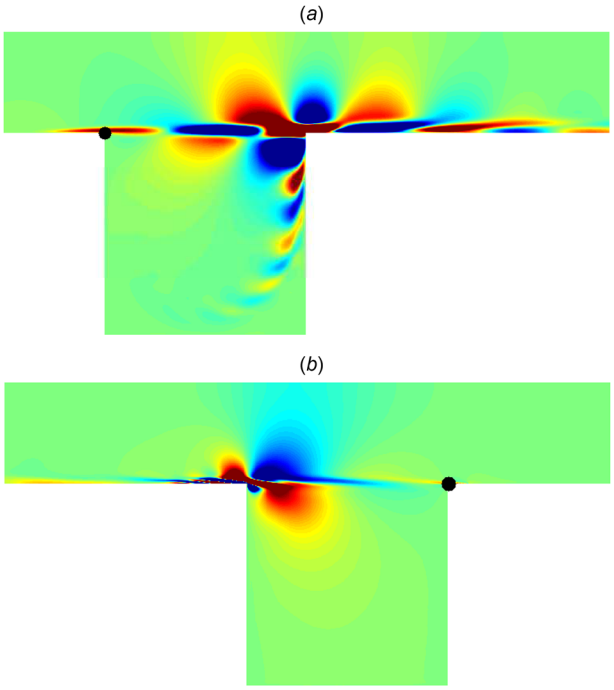

Fig. 6 (*a*) Principal balanced mode and (*b*) associated adjoint balanced mode, visualized by contours of the streamwise velocity component. The actuator and sensor locations are indicated by black symbols.

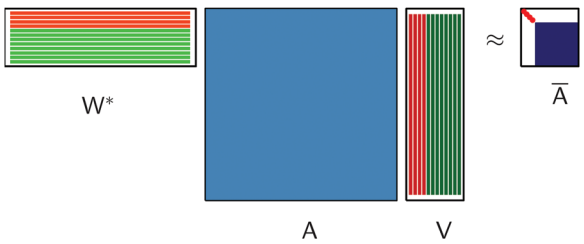

Fig. 7 Sketch of model reduction procedure (Galerkin projection) for the system matrix. Unstable global modes are indicated in red (direct modes in V_u and adjoint modes in W_u), and balanced modes are indicated in green (direct modes in V_s and adjoint modes in W_s). The reduced system matrix $\overline{\mathsf{A}}$ consists of a diagonal submatrix containing the unstable eigenvalues (red symbols) and a dense submatrix (dark blue) describing the reduced stable subspace dynamics.

How to reduce the stable subspace [40,43]?
Linux commands:

1. cd ../ROM
2. FreeFem++-nw direct.edp # solution of the linearized Navier–Stokes equations with an impulse in the control signal $u(t)$
3. FreeFem++-nw adjoint.edp # solution of the adjoint linearized Navier–Stokes equations with an impulse in the measurement signal $y(t)$
4. FreeFem++-nw gramian.edp # build and save the cross-Gramian to disk
5. MATLAB -nodesktop -nosplash < bpod.m # compute balanced modes
6. FreeFem++-nw buildredmat.edp # compute reduced matrices and vectors

Comments. We perform one direct (code Cavity/ROM/direct.edp) and one adjoint (code Cavity/ROM/adjoint.edp) simulation (supplemental material is available under the "Supplemental Data" tab on the ASME Digital Collection):

$$\dot{\mathbf{x}} = \mathsf{A}\mathbf{x}, \quad \mathbf{x}(0) = \mathsf{B}_u^s \tag{13a}$$

$$\dot{\mathbf{y}} = \mathsf{A}^*\mathbf{y}, \quad \mathbf{y}(0) = \mathsf{C}_y^{s,*} \tag{13b}$$

where $\mathsf{B}_u^s = (\mathsf{I} - \mathsf{V}_u\mathsf{W}_u^*)\mathsf{B}_u$ and $\mathsf{C}_y^{s,*} = (\mathsf{I} - \mathsf{W}_u\mathsf{V}_u^*)\mathsf{C}_y^*$ designate the control matrix B_u and estimation measurement matrix C_y projected onto the stable subspace of A and A^*. These codes are based on the spatial and temporal discretization techniques for the DNS code, presented above. The first-order (in time) version of the direct code iteratively solves (matrix inversions are performed with a direct LU solver)

$$\begin{pmatrix} \frac{1}{\Delta t} + (\,)\cdot\nabla\mathbf{u}_0 + \mathbf{u}_0\cdot\nabla(\,) - \nu\Delta(\,) & \nabla(\,) \\ \nabla\cdot(\,) & 0 \end{pmatrix} \begin{pmatrix} \mathbf{u}^{n+1} \\ \mathsf{p}^{n+1} \end{pmatrix} = \begin{pmatrix} \frac{\mathbf{u}^n}{\Delta t} \\ 0 \end{pmatrix} \tag{14}$$

while the adjoint code either solves for the continuous adjoint equations in time

$$\begin{pmatrix} \frac{1}{\Delta t} + (\,)\cdot\nabla\mathbf{u}_0^* - \mathbf{u}_0\cdot\nabla(\,) - \nu\Delta(\,) & \nabla(\,) \\ \nabla\cdot(\,) & 0 \end{pmatrix} \begin{pmatrix} \mathbf{u}^{n+1} \\ \mathsf{p}^{n+1} \end{pmatrix} = \begin{pmatrix} \frac{\mathbf{u}^n}{\Delta t} \\ 0 \end{pmatrix} \tag{15}$$

or considers the transconjugate of the matrix used in the direct solver (code Cavity/ROM/adjoint.edp). Supplemental material is available under the "Supplemental Data" tab on the ASME Digital Collection. Considering a series of M snapshots $(\mathbf{x}(i\Delta t), i = 1..M)$, $(\mathbf{y}(i\Delta t), i = 1..M)$ of these two simulations, we may approximate the controllability and observability Gramians [114] as

$$\mathsf{P} = \int_0^\infty \exp(\mathsf{A}t)\mathsf{B}_u^s\mathsf{B}_u^{s,*}\exp(\mathsf{A}^*t)dt \approx \sum_{i=1}^N \mathbf{x}(i\Delta t)\mathbf{x}(i\Delta t)^*\delta_i = \mathsf{X}\mathsf{X}^* \tag{16a}$$

$$\mathsf{Q} = \int_0^\infty \exp(\mathsf{A}^*t)\mathsf{C}_y^{s,*}\mathsf{C}_y^s\exp(\mathsf{A}t)dt \approx \sum_{i=1}^N \mathbf{y}(i\Delta t)\mathbf{y}(i\Delta t)^*\delta_i = \mathsf{Y}\mathsf{Y}^* \tag{16b}$$

where δ_i refers to quadrature coefficients. A fourth-order Simpson method is commonly used to approximate the integral. We then explicitly form the cross-Gramian $\mathsf{Y}^*\mathsf{X}$ (code Cavity/ROM/gramian.edp) and perform its singular value decomposition (code Cavity/ROM/bpod.m) (supplemental material is available under the "Supplemental Data" tab on the ASME Digital Collection)

$$\mathsf{Y}^*\mathsf{X} = \mathsf{U}\Sigma\mathsf{T}^* \tag{17}$$

where $\mathsf{U}^*\mathsf{U} = \mathsf{I}$ and $\mathsf{T}^*\mathsf{T} = \mathsf{I}$. Σ is a diagonal matrix with positive entries, the Hankel singular values. The bases V_s and W_s are then obtained by retaining only the largest Hankel values in this decomposition and by computing

$$\mathsf{V}_s = \mathsf{X}\mathsf{T}\Sigma^{-1/2}, \quad \mathsf{W}_s = \mathsf{Y}\mathsf{U}\Sigma^{-1/2} \tag{18}$$

Finally, the reduced model $(\overline{\mathsf{A}}, \overline{\mathsf{B}}_u, \overline{\mathsf{C}}_y)$ can be obtained by Galerkin projection (code Cavity/ROM/buildredmat.edp). Supplemental material is available under the "Supplemental Data" tab on the ASME Digital Collection.

3.2 Control Design With Optimal Control. Once the full-scale model has been reduced, we can design a compensator. Combining the two disturbance/noise sources w and g, introduced above, into a composite vector $\mathbf{n} = (g \;\; w)^*$, we can slightly recast the governing equations and state

$$\dot{\overline{\mathbf{x}}} = \overline{\mathsf{A}}\overline{\mathbf{x}} + \overline{\mathsf{B}}_u u + (0 \quad \overline{\mathsf{B}}_u)\mathbf{n} \tag{19a}$$

$$y = \overline{\mathsf{C}}_y\overline{\mathbf{x}} + (1 \quad 0)\mathbf{n} \tag{19b}$$

$$\mathbf{z} = \begin{pmatrix} \overline{\mathsf{C}}_z\overline{\mathbf{x}} \\ \ell u \end{pmatrix} \tag{19c}$$

In addition to a rearrangement of the exogenous noise terms, we have also modified the objective signal by including a fraction of the control signal u. The cost functional or control objective is based on the expected value of this augmented objective signal $\mathbf{z}$

$$\langle \mathbf{z}^*\mathbf{z} \rangle = \langle \overline{\mathbf{x}}^*\overline{\mathsf{C}}_z^*\overline{\mathsf{C}}_z\overline{\mathbf{x}} + \ell^2 u^2 \rangle \tag{20}$$

By extending the previous objective signal by the weighted control signal ℓu, we can regulate the amount of control energy expended by the compensator. For small values of ℓ^2, we expend control efforts rather generously, while for large values of ℓ^2, any control effort is heavily penalized and thus expended rather parsimoniously. The limit of $\ell^2 \to \infty$ is known as the small-gain limit (SGL).

It is apparent from Fig. 5 that the plant produces output (y) from input (u), while the compensator furnishes input (u) from processing the output (y). The task of designing a compensator then lies in the construction of a linear relationship from y to u, represented, for example, by its transfer function K_{uy}, such that the closed-loop transfer-function from the noise signal $\mathbf{n}$ to the objective signal $\mathbf{z}$

$$\overline{\mathsf{T}}_{\mathbf{zn}}^{cl} = \frac{1}{1 - \mathsf{K}_{uy}\overline{\mathsf{T}}_{yu}} \begin{pmatrix} \overline{\mathsf{T}}_{zu}\mathsf{K}_{uy} & \overline{\mathsf{T}}_{zu} \\ \ell\mathsf{K}_{uy} & \ell\mathsf{K}_{uy}\overline{\mathsf{T}}_{yu} \end{pmatrix} \tag{21}$$

obtained by combining in parallel the open-loop transfer function $\overline{\mathsf{T}}_{yu}$ and the compensator, K_{uy}, minimizes a yet to be specified control objective. Inspection of expression $\overline{\mathsf{T}}_{\mathbf{zn}}^{cl}$ shows that the poles of the closed-loop system correspond to the zeros of $1 - \mathsf{K}_{uy}(s)\overline{\mathsf{T}}_{yu}(s)$. Hence, for the closed-loop system to be stable, the compensator is designed to place these zeros into the stable left half-plane. We also note that the poles of the plant and the compensator automatically cancel in $\overline{\mathsf{T}}_{\mathbf{zn}}^{cl}$. For this reason, the poles of a closed-loop system are unconnected to those of either the plant or the compensator, and a closed-loop system may be stable, even though the plant or the compensator exhibits unstable modes.

The control objective may be precisely defined by introducing the normalized disturbance inputs g' and w', with $g = \sqrt{G}g'$ and $w = \sqrt{W}w'$, where $G = \langle gg^* \rangle$ and $W = \langle ww^* \rangle$, respectively, denote the two governing noise covariances: for the sensor noise and for the controller-added noise. Linear-quadratic-Gaussian (LQG)-control stabilizes the compensated system and minimizes (among all possible compensators) the two-norm of the following closed-loop transfer-function $\overline{\mathsf{T}}_{\mathbf{zn}'}^{cl}$ from $\mathbf{n}'$ to $\mathbf{z}$:

$$\dot{\overline{\mathbf{x}}} = \overline{\mathsf{A}}\overline{\mathbf{x}} + \overline{\mathsf{B}}_u u + (0 \quad \sqrt{W}\overline{\mathsf{B}}_u)\mathbf{n}' \tag{22a}$$

$$y = \overline{\mathsf{C}}_y\overline{\mathbf{x}} + (\sqrt{G} \quad 0)\mathbf{n}' \tag{22b}$$

$$\mathbf{z} = \begin{pmatrix} \overline{\mathsf{C}}_z\overline{\mathbf{x}} \\ \ell u \end{pmatrix} \tag{22c}$$

Hence, in the presence of disturbance inputs g and w with covariances G and W, an LQG-controller minimizes the expected value of $\langle \mathbf{z}^*\mathbf{z} \rangle$, which is equal to the (squared) two-norm of the closed-loop transfer function $\overline{\mathsf{T}}_{\mathbf{zn}'}^{cl}$ to be minimized.

Table 1 Performance and robustness measures for the FSC obtained with an LQR, with a partial-state controller (PSC) designed with LQG control and with an $\mathcal{H}_\infty$ IM controller at Re = 7500. The SGL refers to ($\ell^2=\infty$ and $G/W=\infty$), while the MG case is related to ($\ell^2=2041$ and $G/W=1587$). The IM results have been obtained with ($W_y/W_d=10^{-2}$). The gain $GM^{\pm}$ and phase PM margins are given in decibels and degrees, respectively.

	$\|\overline{\mathsf{T}}^{\mathrm{cl}}_{zw}\|_2$	$\|\overline{\mathsf{T}}^{\mathrm{cl}}_{ug}\|_2$	$\|\overline{\mathsf{T}}^{\mathrm{cl}}_{uw}\|_2 = \|\overline{\mathsf{T}}^{\mathrm{cl}}_{zg}\|_2$	GM^+	GM^-	PM	ρ
FSC LQR/SGL	727		2.89	∞	−6.02	60.00	0.500
FSC LQR/MG	95		4.05	∞	−9.94	60.00	0.609
PSC LQG/SGL	2454	0.050	11.26	0.16	−0.26	1.16	0.019
PSC LQG/MG	1636	0.072	8.67	1.17	−1.31	7.83	0.137
PSC IM ($\gamma=\infty$)	1687	3.07	8.44	1.35	−1.20	8.12	0.129
PSC IM ($\gamma=5.91$)	2334	32.4	9.93	1.41	−1.65	9.99	0.173
PSC IM ($\gamma=5.37$)	3612	105	14.08	1.49	−1.79	10.70	0.186

The compensator with a transfer function K_{uy} can be written in state-space form according to

$$\dot{\hat{\mathbf{x}}} = \mathsf{J}\hat{\mathbf{x}} + \mathsf{L}y \tag{23a}$$

$$u = \mathsf{K}\hat{\mathbf{x}} \tag{23b}$$

where $\hat{\mathbf{x}}$ denotes the estimated coefficient vector—expressed in the same basis V and approximating $\overline{\mathbf{x}}$—and L and K are the Kalman and control gains, respectively. L corresponds to the weight factor multiplying any measurement mismatch to accomplish an accurate and reactive estimate of the flow state, while K represents the mapping of the estimated state to the control law. The transfer function associated with the above compensator system is given by

$$\mathsf{K}_{uy}(s) = \mathsf{K}(s\mathsf{I} - \mathsf{J})^{-1}\mathsf{L} \tag{24}$$

The control and Kalman gains K and L are determined from two algebraic matrix Riccati equations [87]. The parameters governing these gains appear in the transfer-function (22), whose two-norm is to be minimized: (i) the noise/disturbance covariances G and W, for which only the ratio G/W is significant and (ii) the parameter ℓ^2 measuring the cost of any control effort. Once K and L are determined, the system matrix J is straightforwardly obtained by $\mathsf{J} = \overline{\mathsf{A}} - \mathsf{L}\overline{\mathsf{C}}_y + \overline{\mathsf{B}}_u\mathsf{K}$. Note that in the SGL ($\ell^2 \to \infty$ and $G/W \to \infty$), the resulting compensator leads to a reflection of the unstable poles about the ($\sigma = 0$) axis.

The performance of the resulting compensator may be assessed by analyzing the four components of the closed-loop transfer function (21). Considering the output u rather than ℓu, we are led to

$$\begin{pmatrix} \overline{\mathsf{T}}^{cl}_{zg} & \overline{\mathsf{T}}^{cl}_{zw} \\ \overline{\mathsf{T}}^{cl}_{ug} & \overline{\mathsf{T}}^{cl}_{uw} \end{pmatrix} = \begin{pmatrix} 1 & 0 \\ 0 & \ell^{-1} \end{pmatrix} \overline{\mathsf{T}}^{cl}_{\mathbf{zn}} \tag{25}$$

The two-norms of these four transfer functions are given in Table 1 for the SGL-case (third line). The transfer functions resulting from the actuator noise w may be compared to those obtained for a full-state controller (FSC) in which the plant-state is assumed to be known, i.e., $u = \mathsf{K}\overline{\mathbf{x}}$. These norms are reported in the second line of the table. It is seen that the estimator component, which is required in the case of a partial-state-controller, is responsible for a considerable loss of performance, both for the expected value of z (increased by a factor of 3.4) and for the expected value of u (increased by a factor of 3.9). We also show in Fig. 8 the two transfer functions related to the sensor noise g, namely, $\overline{\mathsf{T}}^{cl}_{zg}$ and $\overline{\mathsf{T}}^{cl}_{ug}$. Physically, they describe the resulting power spectral density of the performance measurement signal z and of the control signal u, in the presence of white measurement noise g only.

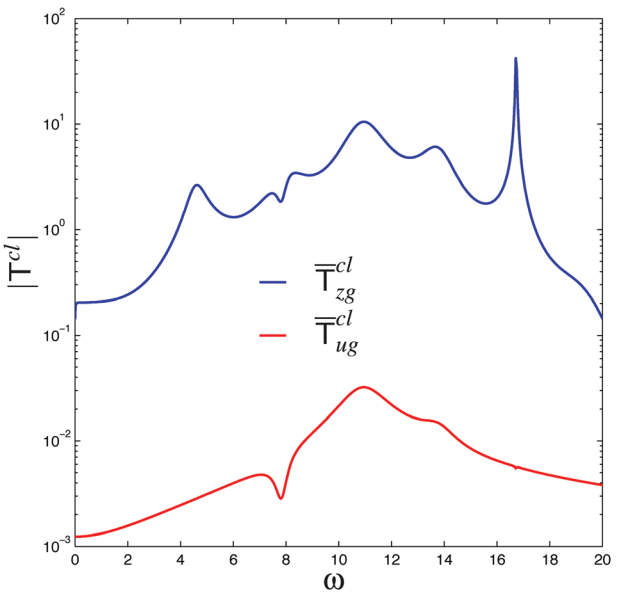

Fig. 8 Modulus of the closed-loop transfer function between sensor noise g and objective signal z (blue curve) and between sensor noise g and control signal u (red curve) for open-cavity flow at Re = 7500 with ($\ell^2 = \infty$ and $G/W = \infty$) (SGL).

How to design an LQG controller and launch a DNS with this controller [43,87]?

Linux commands:

1. cd ../Reg
2. MATLAB -nodesktop -nosplash < h2.m # compute controller
3. cd ../DNSCONTROL
4. FreeFem++-nw init.edp # generate initial condition for the DNS solver
5. FreeFem++-nw dnscontrol.edp # launch DNS with controller designed in../Reg

Comments. The optimization problem for the control gain yields the following algebraic matrix Riccati equation for an auxiliary variable R:

$$\overline{\mathsf{A}}^*\mathsf{R} + \mathsf{R}\overline{\mathsf{A}} - \mathsf{R}\overline{\mathsf{B}}_u\ell^{-2}\overline{\mathsf{B}}^*_u\mathsf{R} + \overline{\mathsf{C}}^*_z\overline{\mathsf{C}}_z = 0 \tag{26}$$

from which the control gain K follows as:

$$\mathsf{K} = -\ell^{-2}\overline{\mathsf{B}}^*_u\mathsf{R} \tag{27}$$

Analogously, the optimization problem for the Kalman gain involves an auxiliary variable S, which is the solution of an algebraic matrix Riccati equation of the form

$$\overline{\mathsf{A}}\mathsf{S} + \mathsf{S}\overline{\mathsf{A}}^* - \mathsf{S}\overline{\mathsf{C}}^*_y\mathsf{G}^{-1}\overline{\mathsf{C}}_y\mathsf{S} + \overline{\mathsf{B}}_w\mathsf{W}\overline{\mathsf{B}}^*_w = 0 \tag{28}$$

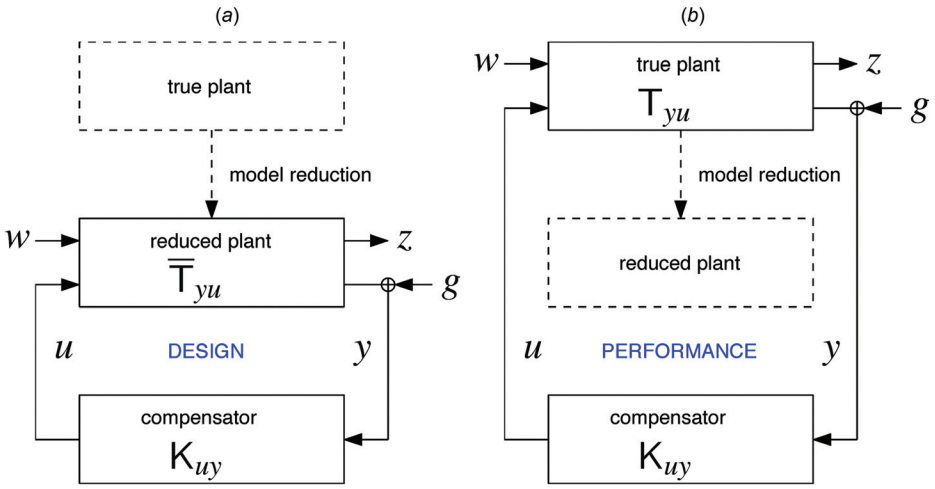

Fig. 9 Block diagram illustrating the compensator design process (*a*) and the application of the reduced-order compensator to the full plant (*b*). The performance and robustness of the design are evaluated for the configuration on the right.

from which the Kalman gain L follows as

$$\mathsf{L} = \mathsf{S}\overline{\mathsf{C}}_y^* \mathsf{G}^{-1} \tag{29}$$

3.3 Closing the Loop With the Large-Scale System: The Robustness Issue. It has to be kept in mind that the compensator is strictly designed for the model-reduced (low-dimensional) fluid system (11), and the stabilization of the plant can only be expected for the reduced-order model. Nonetheless, the reduced-order compensator is applied to the full plant and expected to produce comparable results (see Fig. 9 for a sketch).

In the case of the compensated full plant, the transfer function of the closed-loop system

$$\mathsf{T}_{\mathbf{zn}}^{cl} = \frac{1}{1 - \mathsf{K}_{uy}\mathsf{T}_{yu}} \begin{pmatrix} \mathsf{T}_{zu}\mathsf{K}_{uy} & \mathsf{T}_{zu} \\ \ell\mathsf{K}_{uy} & \ell\mathsf{K}_{uy}\mathsf{T}_{yu} \end{pmatrix} \tag{30}$$

establishing a link between the disturbance input $\mathbf{n}$ and the objective signal $\mathbf{z}$ is similar to the reduced version, $\overline{\mathsf{T}}_{\mathbf{zn}}^{cl}$ (see Eq. (21)), except that the reduced open-loop transfer functions ($\overline{\mathsf{T}}_{yu}$, etc.) are replaced by the equivalent ones for the full plant (T_{yu}, etc.). The reduced and full-plant open-loop transfer functions are generally close to each other (see Sec. 3.1) but never exactly equal. In the case of a minor mismatch, the two-norm of $\mathsf{T}_{\mathbf{zn}'}^{cl}$ will be slightly different from the two-norm of $\overline{\mathsf{T}}_{\mathbf{zn}'}^{cl}$, indicating that the expected value of $\mathbf{z}$ will slightly differ. In the case of a more severe mismatch, the full-plant closed-loop system may even become unstable, with a zero of $1 - \mathsf{K}_{uy}\mathsf{T}_{yu}$ appearing in the unstable half-plane. It is therefore mandatory to evaluate the performances of the reduced-order compensator when applied to the full-plant system. For the present case, results are shown in Fig. 10; both the time-traces of the objective signal z and the control signal u are displayed. After four convective time units, representative of twice the time of travel across the cavity, the objective signal z is successfully damped, confirming that the global instability of the flow at this Reynolds number has been suppressed. Two convective time units are necessary for the estimator to produce accurate and reliable approximations of the flow field from shear measurements y, while two other time units pass before the effect of the control signal u is felt at the downstream sensor location of z. After these four time units, the closed-loop compensator is fully

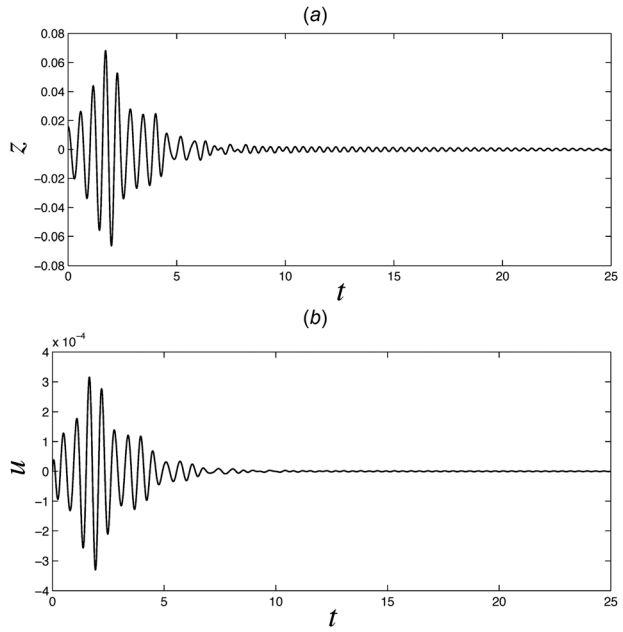

Fig. 10 Objective sensor signal z (*a*) and control signal u (*b*) for compensated flow over an open cavity at Re = 7500 in the SGL. The simulation has been initialized with the most unstable global mode, whose amplitude has been chosen sufficiently small such that the entire simulation remains in the linear regime. No disturbance/noise sources w and g have been applied.

operative and successful in eliminating the instability and minimizing the objective signal. In summary, the compensator—designed for a reduced-order model of the full system in the SGL—has been applied to the full system and has proven successful in suppressing the inherent flow instabilities at a Reynolds number of Re = 7500. We will next take a closer look at this performance and determine the limiting margins of our design before instabilities *in the closed-loop system* render the compensator ineffective. Two cases will be considered for an analysis of our closed-loop dynamics in off-design operation: (i) a shift in Reynolds number and (ii) the excitation of nonlinear effects.

3.4 Robustness to a Shift in Reynolds Number. In a first experiment to determine the margins of stability for the closed-

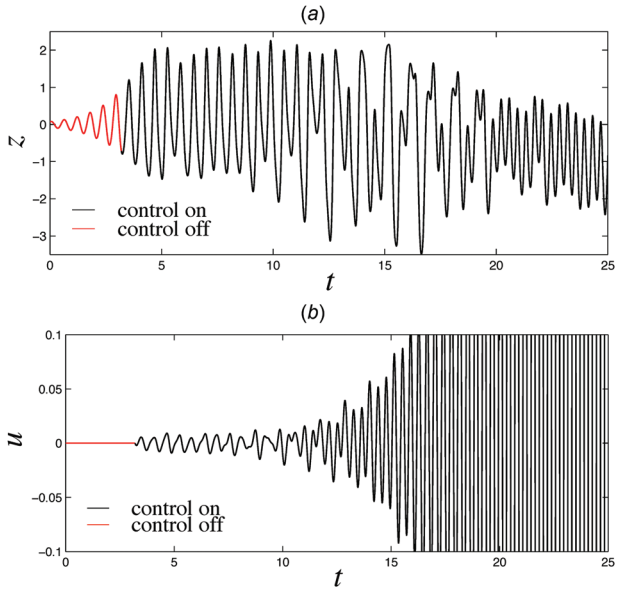

Fig. 11 Objective sensor signal *z* (*a*) and control signal *u* (*b*) for compensated flow over an open cavity applying a compensator designed for Re = 7500 in the SGL to a flow at a Reynolds number of Re = 7000. The initial condition consists of the most unstable global mode, with a sufficiently low amplitude for the simulation to remain in the linear regime.

loop system, we apply the compensator, designed for stabilizing the flow at a Reynolds number of Re = 7500, to flow over the same cavity at a Reynolds number of Re = 7000. As before, the SGL has been invoked which results in a parsimonious control effort to achieve the control objective. The objective signal z and the control signal u are given in Fig. 11. It is clear that the compensator could not stabilize the flow at Re = 7000, as evidenced by the rapidly diverging control signal u and the unsettled objective signal z. It appears that the Re = 7500 compensator does not possess sufficient robustness to negotiate this rather small change in Reynolds number.

We will take a closer look at robustness issues and introduce generic perturbations $\Delta(s)$ to the reduced transfer function $\overline{\mathsf{T}}_{yu}(s)$, such that

$$\mathsf{T}_{yu}(s) = [1 + \Delta(s)]\overline{\mathsf{T}}_{yu}(s) \tag{31}$$

A sketch of the perturbed closed-loop system is given in Fig. 12. We will follow a classical path and track the unstable poles of the closed-loop transfer function given in Eq. (30)—which is equivalent to tracing the unstable zeros of the expression $1 - \mathsf{K}_{uy}\mathsf{T}_{yu}$. By design, we know that all zeros of $1 - \mathsf{K}_{uy}\overline{\mathsf{T}}_{yu}$ are located in the stable half-plane. The smallest perturbation $\Delta(s)$ to the reduced transfer function $\overline{\mathsf{T}}_{yu}$ that yields a marginal zero in this expression provides a measure of stability margin for the closed-loop system.

First, to simplify the analysis, we will consider modifications to the open-loop transfer function $\overline{\mathsf{T}}_{yu}$ in the form of a multiplicative complex factor $1 + \Delta(s) = g$. We therefore introduce a modified transfer function T_{yu} according to

$$\mathsf{T}_{yu} = g\overline{\mathsf{T}}_{yu} \qquad g \in \mathbb{C} \tag{32}$$

and assess the movement of the zeros of $1 - g\mathsf{K}_{uy}\overline{\mathsf{T}}_{yu}$ as g is varied. Further simplifications are put forth: (i) a purely real and positive change in $g = a$, i.e., $a \in \mathbb{R}^+$ and (ii) a change in the phase of g of the form $g = \exp(i\phi)$. The special case $g = 1$ recovers the stable configuration (by design) of the small-gain compensated, closed-loop system. By varying g, we probe the stability margins of the closed-loop system with respect to structured changes in the

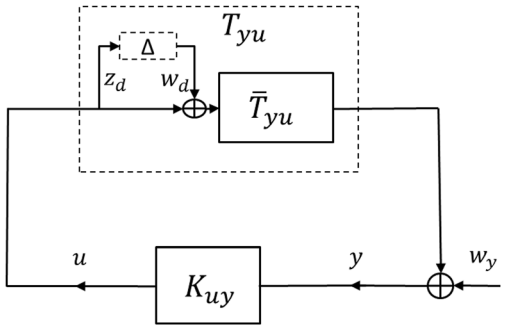

Fig. 12 Closed-loop perturbed system. The closed-loop system is composed of the actual cavity flow T_{yu} and the controller K_{uy}. The actual transfer function T_{yu} is slightly different from the reduced transfer function $\overline{\mathsf{T}}_{yu}$ by a multiplicative factor $1+\Delta$. The perturbation Δ displays one input (the control signal $z_d = u$) and one output (the actuator noise w_d). We have also indicated an additional input to the closed-loop system, w_y, which is required for well-posedness of the $\mathcal{H}_\infty$ design framework.

system to be controlled [87]. Physically, the first case $g \in \mathbb{R}^+$ models an estimation error in the instability's amplification rate, while the second case $g = \exp(i\phi)$ represents an estimation error in the instability's convection speed. In the former case, two margins arise: one for a minimum underestimation of the instability's amplification rate, denoted by $a^- < 1$, and one for a maximum overestimation, represented by $a^+ > 1$. Traditionally, these two *gain margin* (GM) values are expressed in decibels (dB) and abbreviated as $\mathrm{GM}^+ = 20\log_{10}a^+$ and $\mathrm{GM}^- = 20\log_{10}a^-$. In the latter case, the minimum positive angle ϕ (denoted ϕ^+) yielding closed-loop instability corresponds to the PM and is given in degrees.

A more general way to assess robustness is to consider a completely generic perturbation Δ and determine the perturbation Δ of smallest norm (here the infinity-norm) that yields closed-loop instability. Considering the actuator noise input w_d and control signal output $z_d = u$ of the unperturbed closed-loop system, the small-gain-theorem [87] demonstrates that the perturbed closed-loop system (with $\overline{\mathsf{T}}_{yu}$, K_{uy}, and Δ all connected as shown in Fig. 12) is stable if and only if

$$|\Delta(i\omega)| \le \frac{1}{\left|T^{cl}_{z_d w_d}(i\omega)\right|}, \quad \forall\omega \tag{33}$$

where

$$T^{cl}_{z_d w_d}(s) = \frac{K_{uy}(s)\overline{\mathsf{T}}_{yu}(s)}{1 - K_{uy}(s)\overline{\mathsf{T}}_{yu}(s)} \tag{34}$$

is the transfer function of the unperturbed closed-loop system from the input w_d to the output z_d. The latter expression is also known from the literature as the complementary sensitivity function [94]. This result implies that the system becomes unstable if there exists a frequency where the product of the perturbation amplitude $|\Delta|$ and the closed-loop transfer function amplitude $|T^{\mathrm{cl}}_{z_d w_d}|$ is larger than 1. From this, a new global robustness measure may be defined: considering the quantity ρ such that

$$\rho = \frac{1}{\|T^{\mathrm{cl}}_{z_d w_d}(s)\|_\infty} \tag{35}$$

the small-gain theorem states that the closed-loop system is stable if and only if $\|\Delta\|_\infty \le \rho$. We recall the definition of the infinity-norm: $\|T\|_\infty \equiv \sup_\omega |T(i\omega)|$.

The small-gain theorem also provides us with a method to better analyze the frequencies where a perturbation Δ may most

easily render the closed-loop system unstable. Introducing the amplitude a and phase ϕ satisfying $\mathsf{T}_{yu} = ae^{i\phi}\overline{\mathsf{T}}_{yu}$, closed-loop stability requires that

$$\underbrace{\max\left(0, 1 - \frac{1}{|T^{\mathrm{cl}}_{z_d w_d}(i\omega)|}\right)}_{a^-(\omega)} \le a \le \underbrace{1 + \frac{1}{|T^{\mathrm{cl}}_{z_d w_d}(i\omega)|}}_{a^+(\omega)} \tag{36}$$

$$|\phi| \le \underbrace{\arccos\left(1 - \frac{1}{2|T^{\mathrm{cl}}_{z_d w_d}(i\omega)|^2}\right)}_{\phi^+(\omega)} \tag{37}$$

The margins $a^+(\omega)$, $a^-(\omega)$, and $\phi^+(\omega)$ provide gain and PM which depend on the frequency, in contrast to the previously introduced margins a^+, a^-, and ϕ^+. They provide additional insight into the critical frequencies where the perturbation Δ might most easily destabilize the closed-loop system.

Analysis of the robustness margins $\mathrm{GM}^+, \mathrm{GM}^-, \mathrm{PM}$, and ρ for our above SGL-case at $\mathrm{Re} = 7500$ reveals exceedingly small margins. These numbers, which are reported in Table 1 (third line, labeled "PSC LQG/SGL"), show that only a minute error of less than 2% is tolerable in the estimation of the transfer function, before an eigenvalue of the closed-loop system re-enters the unstable half-plane and renders the compensator ineffective. Recalling the earlier example, it appears that a simple change in the Reynolds number from the design value of $\mathrm{Re} = 7500$ to $\mathrm{Re} = 7000$ has been sufficient to exceed these margins. In Fig. 13(*a*), we have plotted the magnitude of the transfer function $\overline{\mathsf{T}}_{yu}$ for $\mathrm{Re} = 7500$, and the upper $a^+(\omega)$ and lower $a^-(\omega)$ GM are obtained with the SGL-compensator. For stability of the closed-loop system, the perturbed transfer function (e.g., arising from a change in the Reynolds number from $\mathrm{Re} = 7500$ to $\mathrm{Re} = 7000$) must entirely fall within the upper and lower bounds displayed in the figure. We observe that the transfer function for $\mathrm{Re} = 7000$ (red line) exceeds the tight bounds near $\omega \approx 16.9$. This provides graphical confirmation that even a small change in the transfer function can result in closed-loop instabilities, as observed in Fig. 11.

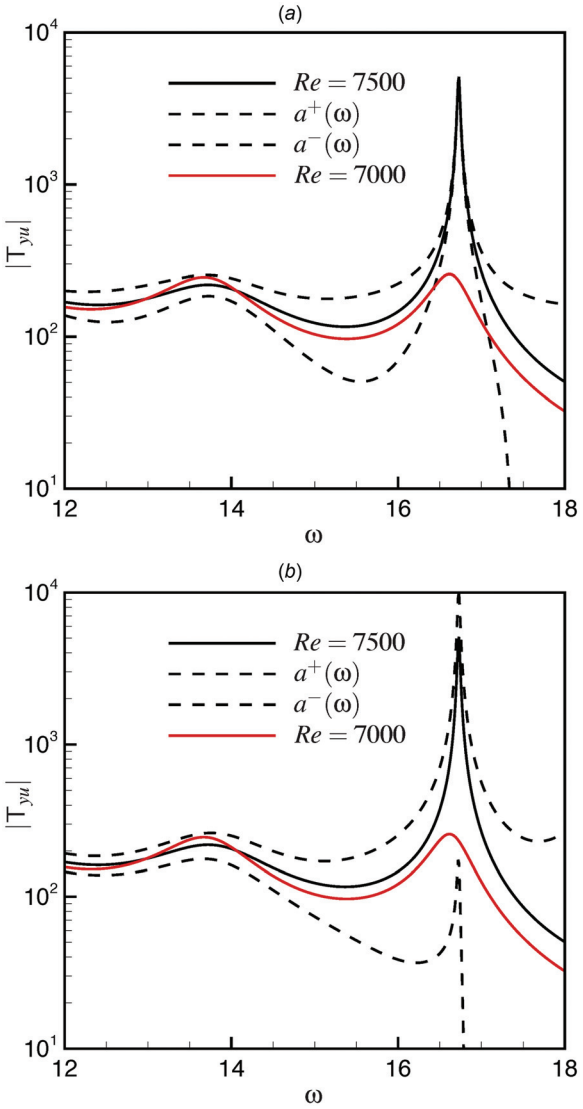

Fig. 13 Modulus of the open-loop transfer function T_{yu} (solid black line), including GM $a^+(\omega)$ and $a^-(\omega)$ (dashed lines), for flow over an open cavity at $\mathrm{Re} = 7500$ stabilized by (*a*) an SGL-compensator and (*b*) an MG-compensator. Note that the open-loop transfer function for $\mathrm{Re} = 7000$, included in red, is contained within the bounds over the entire frequency range only for the MG-compensator.

3.5 Robustness Analysis and Improvements. The stability margins depend on the parameters ℓ^2 and G/W which determine the control gain and Kalman gain. Taking the SGL, $\ell^2 \to \infty$ and $G/W \to \infty$, resulted in the expenditure of only a minimal control effort (only the unstable structures have nonzero, but small gains) and the minimal adjustment of the estimator by measurement mismatch (case of very noisy sensors). In this limit, the compensator displays weak robustness, which itself has not been explicitly enforced. In an effort to increase the stability margins, we relax the SGL in the design of the Kalman filter and apply a loop-shaping technique known as LTR.

FSC (linear-quadratic regulators (LQR)) do not suffer from such small robustness margins; by analyzing the appearance of marginal zeros of the loop transfer-function $1 - g\mathsf{K}\overline{\mathsf{T}}_{\mathbf{x}u}$ as a function of g, it may be shown [87] that they exhibit at least $\mathrm{GM}^+ = \infty$, $\mathrm{GM}^- = -6\,\mathrm{dB}$, a PM of 60deg, and $\rho = 0.5$. The actual GM of the FSC in the SGL case have been computed and reported in Table 1 (line 1, labeled "FSC LQR/SGL"), where it is seen that we precisely recover these theoretical values. It is the estimator component of the LQG-compensator that is responsible for the loss of robustness. LTP attempts to alter the estimator in the LQG-design to more closely resemble an LQR-setup and thus recover the favorable robustness properties of FSC. This can be accomplished by overwhelming the control signal u, which enters the estimator, by an additional and fictitious control noise w. The estimator will then rely far more on the measurement than on the corrupted plant dynamics. This additional noise will produce a larger Kalman gain L and thus a faster estimator whose intrinsic dynamics becomes less prominent. If we obtain an ultrafast estimator, the estimated state $\hat{\mathbf{x}}$ will be equal to the actual state $\overline{\mathbf{x}}$, so that the control signal $u = \mathsf{K}\hat{\mathbf{x}}$ is equal to the full-state control signal $u = \mathsf{K}\overline{\mathbf{x}}$. In other words, by increasing the fictitious control noise input we approach the LQR compensator. Suffice it to mention that the fictitious control noise is merely added during the design procedure of the Kalman gain, i.e., in the algebraic Riccati equation. The new-found Kalman gain L then replaces the original gain.

Adding control noise to the estimator in an effort to approach the LQR-limit yields the sought-after increase in robustness and GM, but at the expense of compensator performance. There is a monotonic increase in the cost functional with increasing spectral density of the fictitious noise in the design process. This trade-off therefore requires a user-supplied compromise between performance and robustness.

Figure 14 displays the $\mathrm{GM}^{\pm}$ (in dB) and PM (in degrees) as a function of the noise covariance ratio G/W and the cost of control ℓ^2 for a compensator designed at $\mathrm{Re} = 7500$. The SGL is located

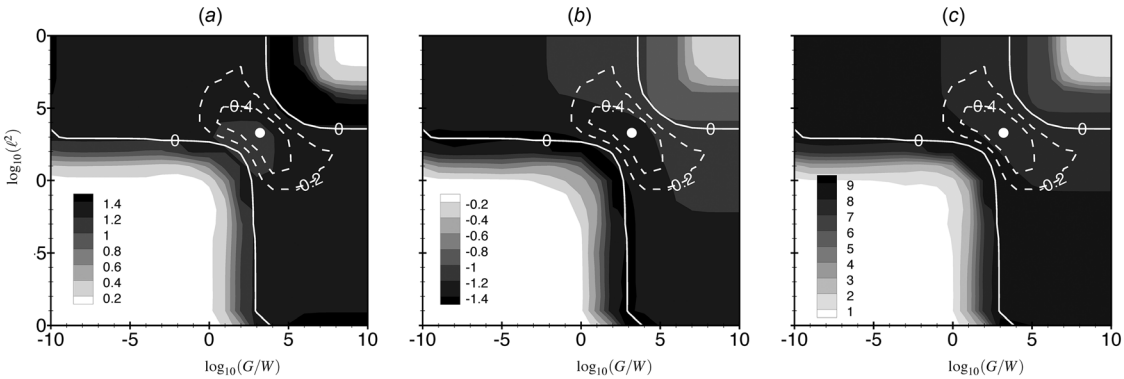

Fig. 14 Contours of gain margins GM^+ (*a*) and GM^- (*b*) and PM (*c*) in the $\log_{10}(G/W)-\log_{10}(\ell^2)$ plane for flow over an open cavity at Re = 7500. Dark contours indicate good robustness properties. The white contour levels represent the least stable eigenvalue of the flow-field at Re = 7000 coupled to a compensator designed at Re = 7500. The white bullet point indicates the coordinates $(G/W = 1587-\ell^2 = 2041)$ corresponding to the LTR calculations.

in the upper right corner, showing small margins in all the three cases as observed previously. For finite and moderate values of these two parameters, a noticeable increase in all the three margins—and therefore a noticeable increase in robustness—can be observed. Notice, however, that the desirable robustness properties of the full-state LQR controller have not been reached. This issue will be discussed below in Sec. 3.9.

Returning to our example of controlling the plant at Re = 7000 with a compensator designed for Re = 7500 we also include in Fig. 14 isocontours of the principal eigenvalue of the closed-loop Re = 7500/7000 system. This eigenvalue corresponds to the least-damped zero of $1 - \mathsf{K}_{uy}|^{\mathrm{Re}=7500}_{G/W,\ell^2}\overline{\mathsf{T}}_{yu}|^{\mathrm{Re}=7000}$. The gray margin contours represent robustness, while the eigenvalue isocontours are concerned with the stability of the compensated system. We can deduce from these figures that, while the closed-loop Re = 7500/7000 system could not be stabilized in the SGL (recall Fig. 11), the improved GM for more modest values of G/W and ℓ^2 lead to the stabilization of the closed-loop system by an off-design compensator. This can also be confirmed by considering the compensator obtained for the parameter values of $G/W = 1587$ and $\ell^2 = 2041$ (the white symbol in Fig. 14). We observe vastly improved gain and PM, which are reported in Table 1 (line 4, labeled "PSC LQG/MG"). The open-loop transfer function $\overline{\mathsf{T}}_{yu}$ for Re = 7500, including the upper and lower bounds $a^+(\omega)$ and $a^-(\omega)$, is presented in Fig. 13(*b*). We see that the open-loop transfer function for Re = 7000 (red line) is now fully contained within the bounds over the entire frequency range. Ultimate confirmation comes from plotting the objective signal z and the control signal u for the case of combining a flow at Re = 7000 with the above LTR-compensator designed for Re = 7500. The results are shown in Fig. 15. In accordance with our conclusions from Fig. 13(*b*), the LTR-compensator succeeds in stabilizing the unstable Re = 7000 flow, even though it has been designed for a flow at Re = 7500. This can be attributed to the improved robustness properties of the LTR-compensator. The performance, however, is suboptimal which is reflected in the slower relaxation to a stable state in Fig. 15.

In summary, loop-shaping techniques have been effective in significantly increasing the gain and PM associated with the SGL. This has been accomplished by an artificially increased control-noise input during the design process which pushed the SGL-compensator gradually toward a full-state (LQR) configuration. It was thus possible, though less efficient, to stabilize the cavity flow at Re = 7000, even with a compensator designed for an operating Reynolds number of Re = 7500.

3.6 Control Design Targeting Stability Robustness. In this section, we design a controller $K_{uy}(s)$ which aims at maximizing

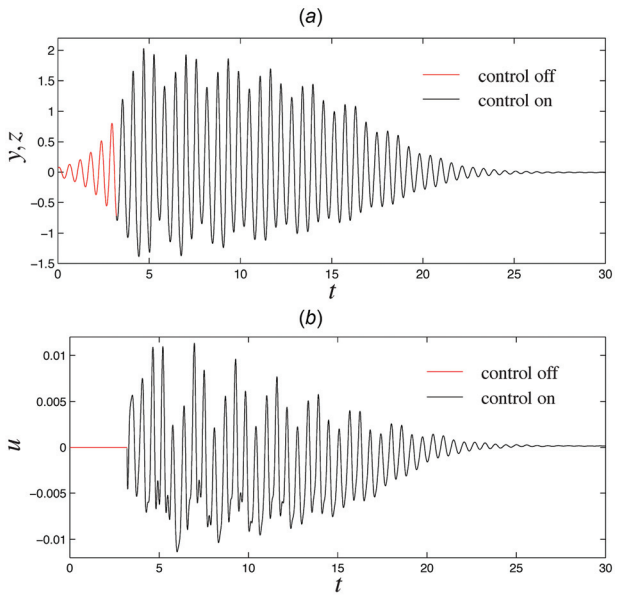

Fig. 15 Time signal of objective measurement *z* (*a*) and control *u* (*b*) for cavity flow at Re = 7000 stabilized by an LTR-compensator designed for Re = 7500

the robustness measure $\rho = \|T^{\mathrm{cl}}_{z_d w_d}\|^{-1}_\infty$, while keeping the closed-loop system stable. To this end, we try to minimize the $\infty-$ norm of the closed-loop transfer function $T^{\mathrm{cl}}_{z_d w_d}$. We consider the reduced model governing the flow field with two outputs, y and z_d, and three inputs, namely, the control signal u, the input w_d of amplitude W_d corrupting the actuator signal, and the input w_y of amplitude W_y contaminating the measurement signal y. Introducing the normalized inputs w'_d and w'_y, such that $w_d = W_d w'_d$ and $w_y = W_y w'_y$, the governing equations read

$$\dot{\overline{\mathbf{x}}} = \overline{\mathsf{A}}\overline{\mathbf{x}} + \overline{\mathsf{B}}_u u + (0 \quad \overline{\mathsf{B}}_u\sqrt{W_d})\mathbf{n}' \tag{38a}$$

$$y = \overline{\mathsf{C}}_y\overline{\mathbf{x}} + (\sqrt{W_y} \quad 0)\mathbf{n}' \tag{38b}$$

$$z_d = u \tag{38c}$$

with $\mathbf{n}' = (w'_y \quad w'_d)^*$. The $\mathcal{H}_\infty$ -control theory provides tools to minimize $\|T^{\mathrm{cl}}_{z_d\mathbf{n}'}\|_\infty$. The optimal controller is obtained by an iterative procedure, where a design parameter γ is progressively decreased. The following upper bound holds for all the values of

γ: $\|T^{\mathrm{cl}}_{z_d \mathbf{n}'}\|_\infty \leq \gamma$. A stopping criterion then provides the smallest possible parameter $\gamma = \gamma_{\min}$, which can be shown to correspond to $\|T^{\mathrm{cl}}_{z_d \mathbf{n}'}\|_\infty$. To recover the previously introduced robustness objective $\|T^{\mathrm{cl}}_{z_d w_d}\|_\infty$, we consider amplitudes W_y of the input w_y that are small compared to the amplitudes W_d of the input w_d: if $W_y/W_d \ll 1$, we obtain $\|T^{\mathrm{cl}}_{z_d \mathbf{n}'}\|_\infty \approx \|T^{\mathrm{cl}}_{z_d w_d}\|_\infty$.

In Table 1, we show in lines 5, 6, and 7, labeled "PSC IM," the performance and robustness measures are obtained for $\gamma = \infty$, $\gamma = 5.91$, and $\gamma = \gamma_{\min} = 5.37$ at a Reynolds number of $\mathrm{Re} = 7500$. We see that the various robustness margins are all increased with respect to the previous controllers, but that the performance criteria further deteriorate. We verified (not shown here) that the linearized numerical simulations with these new controllers also manage to stabilize the base flow at $\mathrm{Re} = 7000$.

For the rest of the paper, we will disregard these controllers and instead focus our attention on LTR controllers (the main conclusions were overall identical for the LTR medium-gain (MG)-controller and the $\mathcal{H}_\infty$ -controllers targeting stability robustness).

How to design a robust controller within the $\mathcal{H}_\infty$-control framework [87]? Linux commands:

1. cd ../Reg
2. MATLAB -nodesktop -nosplash < hinf-im-10percent.m # compute controller
3. cd ../DNSCONTROL
4. FreeFem++-nw init.edp # generate initial condition for DNS solver
5. FreeFem++-nw dnscontrol.edp # launch DNS with controller designed in ../Reg

Comments. The procedure consists of finding the smallest value of $\gamma > 0$, such that

$$\overline{\mathsf{A}}^*\mathsf{R} + \mathsf{R}\overline{\mathsf{A}} - (1-\gamma^{-2})\mathsf{R}\overline{\mathsf{B}}_u\overline{\mathsf{B}}_u^*\mathsf{R} = 0 \tag{39a}$$

$$\overline{\mathsf{A}}\mathsf{S} + \mathsf{S}\overline{\mathsf{A}}^* - (W_y/W_d)^{-1}\mathsf{S}\overline{\mathsf{C}}_y^*\overline{\mathsf{C}}_y\mathsf{S} + \overline{\mathsf{B}}_u\overline{\mathsf{B}}_u^* = 0 \tag{39b}$$

and such that all eigenvalues of RS fall below γ^2 in modulus. The controller may then be computed as follows:

$$K = -\overline{\mathsf{B}}_u^*\mathsf{R} \tag{40a}$$

$$L = (\mathsf{I} - \gamma^{-2}\mathsf{SR})^{-1}\mathsf{S}\overline{\mathsf{C}}_y^*(W_y/W_d)^{-1} \tag{40b}$$

$$J = \overline{\mathsf{A}} + (1-\gamma^{-2})\overline{\mathsf{B}}_u\mathsf{K} - \mathsf{L}\overline{\mathsf{C}}_y \tag{40c}$$

The $\mathcal{H}_\infty$-control framework ensures that $\|T^{\mathrm{cl}}_{z_d \mathbf{n}'}\|_\infty < \gamma$ and that $\|T^{\mathrm{cl}}_{z_d \mathbf{n}'}\|_\infty = \gamma = \gamma_{\min}$ when the eigenvalue criterion is reached.

3.7 Robustness to Nonlinearities. In a second robustness study, we subject the open cavity flow to increasing amplitudes of the initial condition, thus triggering nonlinear effects. For sufficiently large amplitudes, the linear instabilities will eventually saturate into a limit-cycle behavior, characterized by a robust periodic flow pattern. Our first experiment contrasts the control performance of the SGL-compensator with a compensator robustified using LTR for increasing amplitudes of the initial condition at $\mathrm{Re} = 7500$. The results are shown in Fig. 16. For rather low amplitudes, both the SGL- and LTR-compensators are able to render the closed-loop system stable. Due to the reduced gain and PM, however, the SGL-compensator fails rather quickly in stabilizing the system for slightly larger initial amplitudes; the more robust LTR-compensator, on the other hand, is still effective at these amplitudes. Once the amplitudes exceed a critical threshold, however, the LTR-compensator fails as well, and an unstable closed-loop system results.

Nonlinear effects, and the associated limit-cycle behavior, are more prominent for higher Reynolds number. Once the critical

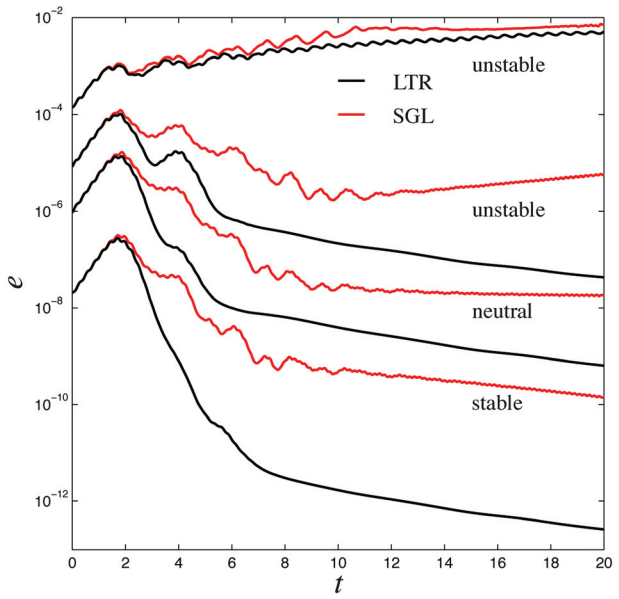

Fig. 16 Temporal evolution of the perturbation kinetic energy for increasing amplitudes of the initial condition, contrasting the performance of SGL-compensation and robustified LTR-compensation ($G/W = 1587 - \ell^2 = 2041$), for cavity flow at $\mathrm{Re} = 7500$

Reynolds number $\mathrm{Re}_c = 4140$ is surpassed, global linear instabilities arise which will be counterbalanced by a saturating effect from the nonlinear terms of the governing equations. This balance leads to a characteristic limit-cycle behavior; the amplitude A of the limit-cycle can be estimated as $A \sim \sqrt{\mathrm{Re} - \mathrm{Re}_c}$. It is interesting to assess the ability of the compensator, designed for the linear regime, to restabilize the flow once it has gone into a limit-cycle behavior. This is, again, a robustness issue: we are applying a compensator to a system in an off-design arrangement.

It was confirmed (not shown here) that an FSC manages to restabilize a limit-cycle behavior up to $\mathrm{Re} = 7500$. In the case of partial-state control, it was not possible to find parameters $(\ell^2, G/W)$ for which the compensators successfully restabilize the limit-cycles for $\mathrm{Re} \geq 7000$. A more favorable configuration is obtained by considering a lower Reynolds number: in this case, the instability is weaker and the amplitude of the limit-cycle is smaller. For $\mathrm{Re} = 6000$, we display the objective measurement z and the corresponding control signal u for both an SGL-compensator and an LTR-compensator. In both cases, control is applied after the fluid system settles into a limit-cycle behavior (see Figs. 17(*a*) and 17(*c*)), and in both cases the control efforts succeed in suppressing the saturated limit-cycle and return the flow to the steady base flow. In the case of the SGL-compensator, we observe a slow but steady decay of the objective signal z, once the control is applied. In contrast, the LTR-compensator, which has been designed for $G/W = 250$ and $\ell^2 = 200$ resulting in $\mathrm{GM}^+ = 2.57\,\mathrm{dB}$, $\mathrm{GM}^- = -3.19\,\mathrm{dB}$, and $PM = 17.9\mathrm{deg}$, shows a significantly more rapid return to the steady base flow which is accomplished with a shorter, but markedly larger control input u (see Figs. 17(*b*) and 17(*d*)).

3.8 Effect of Reynolds Number and Estimation Sensor Location on Robustness Margins. In the absence of an estimator, when full-state information control is applied, the GM are far larger allowing for optimal performance without restrictive robustness constraints. We recall that an FSC manages to restabilize a flow in a limit-cycle for Reynolds numbers up to $\mathrm{Re} = 7500$. Introducing an estimator thus has to be considered as the weak link in the closed-loop system, responsible for the loss of robustness and forcing us into a compromise between performance and

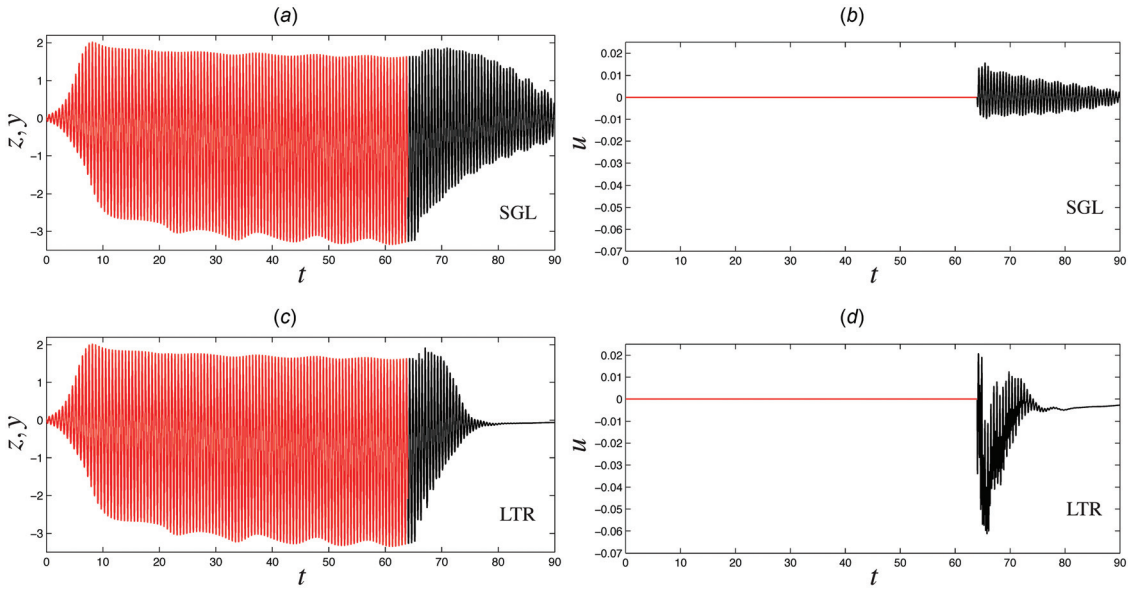

Fig. 17 Objective measurement $z = y$ ((*a*) and (*c*)) and associated control signal u ((*b*) and (*d*)) for control of an open cavity flow at Re = 6000. (*a*) and (*b*) SGL-compensator ($l^2 = \infty$ and $G/W = \infty$). (*c*) and (*d*) LTR-compensator with ($l^2 = 200$ and $G/W = 250$).

robustness which can ameliorate the control problem, but (as we have seen) ultimately not solve it.

There are two main parameters that have a strong impact on the GM: the Reynolds number and the location of the estimation sensor. Indeed, it seems intuitive that in order to provide an effective and robust control, an accurate estimated state $\hat{\mathbf{x}}$ is required to be passed on to the optimal controller; it is equally intuitive that this estimation becomes increasingly difficult as the perturbation growth between input and output becomes more pronounced and as the distance, and therefore the delay, between input and output increases. For example, in the case where no delay exists between input and output, the effect of the control input u is immediately felt by the estimation sensor y, so that only minute discrepancies between the expected and the actual values of the sensor signal y (due to inaccuracies in the model between the dynamics from u to y) are detected and used to correct the estimated state. In the case of a delay between u and y, errors between the expected and the actual value of y will be seen after some delay and will therefore be much stronger (especially in the case of a strong amplification between u and y). Hence, the readjustment of the estimated state toward the actual state will be more violent and may fail: the compensator is less robust as a consequence.

The effect of the Reynolds number on the impulse responses and on the GM is analyzed first. Figures 18(*a*)–18(*d*) presents the impulse responses for Re = 7500, 7000, 6000, and 5250: it shows a constant delay between actuator and sensor, but a rapidly decreasing amplitude due to a decrease in the growth rate of the most unstable mode. The GM^- (representative for the other two margins) for varying Reynolds numbers are shown in Figs. 19(*a*)–19(*d*) as gray contours in the $\log_{10}(G/W) - \log_{10}(\ell^2)$ plane; the gray map is constant across the subplots to allow direct comparison. While we recognize the typical loss of robustness in the small-gain ($G/W \to \infty$ and $\ell^2 \to \infty$) and large-gain ($G/W \to 0$ and $\ell^2 \to 0$) limit, we also observe a definite deterioration of the GM for increasing Reynolds number, making it progressively difficult to achieve a stable closed-loop system. While for Re = 5250, a GM of −6 dB is feasible, for Re = 7500 only about −1.5 dB is attainable. For slightly supercritical Reynolds numbers (and weak amplification between u and y), the favorable stability margins of the full-state LQR controller may thus be recovered.

Next, we will investigate the effect of the estimation sensor location on the GM. For this, we vary the actuator–sensor distance by moving the estimation sensor y (located initially near the downstream edge of the cavity) toward the actuator. When the measurements are performed in the bulk of the flow, the signal y extracts the cross-stream velocity component of the perturbation rather than the shear stress. We choose a Reynolds number of Re = 7000 and consider a sensor located at $x_s = 0.75$, $x_s = 0.5$, $x_s = 0.25$, and $x_s = 0.15$. We recall that in this coordinate system, the actuator is located near $x = -0.1$. The impulse responses for the different sensor locations shown in Figs. 18(*e*)–18(*h*) reflect the fact that information from the actuator reaches the sensor earlier (and also, as a consequence, had less time/distance to grow to larger amplitudes). As for the robustness properties, we focus again on the GM^- in the $\log_{10}(G/W) - \log_{10}(\ell^2)$ plane. The results are shown in Figs. 19(*e*)–19(*h*). The color contours are the same across all subplots, which allows direct comparison. We observe a clear improvement of the GM as the estimation sensor is moved progressively toward the actuator location, thus facilitating a more accurate estimate of the flow state from the measurements that, in turn, is used by the actuator. A gain margin of $GM^- \approx -2$ dB can be tripled to $GM^- \approx -6$ dB by simply displacing the original sensor from $x_s = 0.75$ to $x_s = 0.15$. We note that (even in the case of high Reynolds numbers and strong amplification between u and y) one may recover the favorable robustness margins of the full-state LQR controller when the estimation sensor is moved toward the actuator, i.e., when reducing the delay between u and y.

We have seen that for increasing amplification between u and y, the GM decline precipitously in the case of large delays between u and y (estimation sensor located at the downstream edge). The same trend is observed for increasing delays between u and y in the case of strong amplification between u and y. Hence, the combination of amplification (high Reynolds numbers) and delay (downstream estimation sensor) between inputs and outputs is strongly detrimental to the robustness of the compensator. We will next relate the delays between u and y to unstable zeros of the open-loop transfer function $\overline{\mathsf{T}}_{yu}$.

3.9 Zeros of the Open-Loop Transfer Function $\overline{\mathsf{T}}_{yu}$ and Delays. For the present open-cavity configuration, we now address the existence and significance of unstable zeros in the plant dynamics. The zeros of the open-loop transfer function $\overline{\mathsf{T}}_{yu}$ are displayed for different Reynolds numbers in Fig. 18(*e*) and for

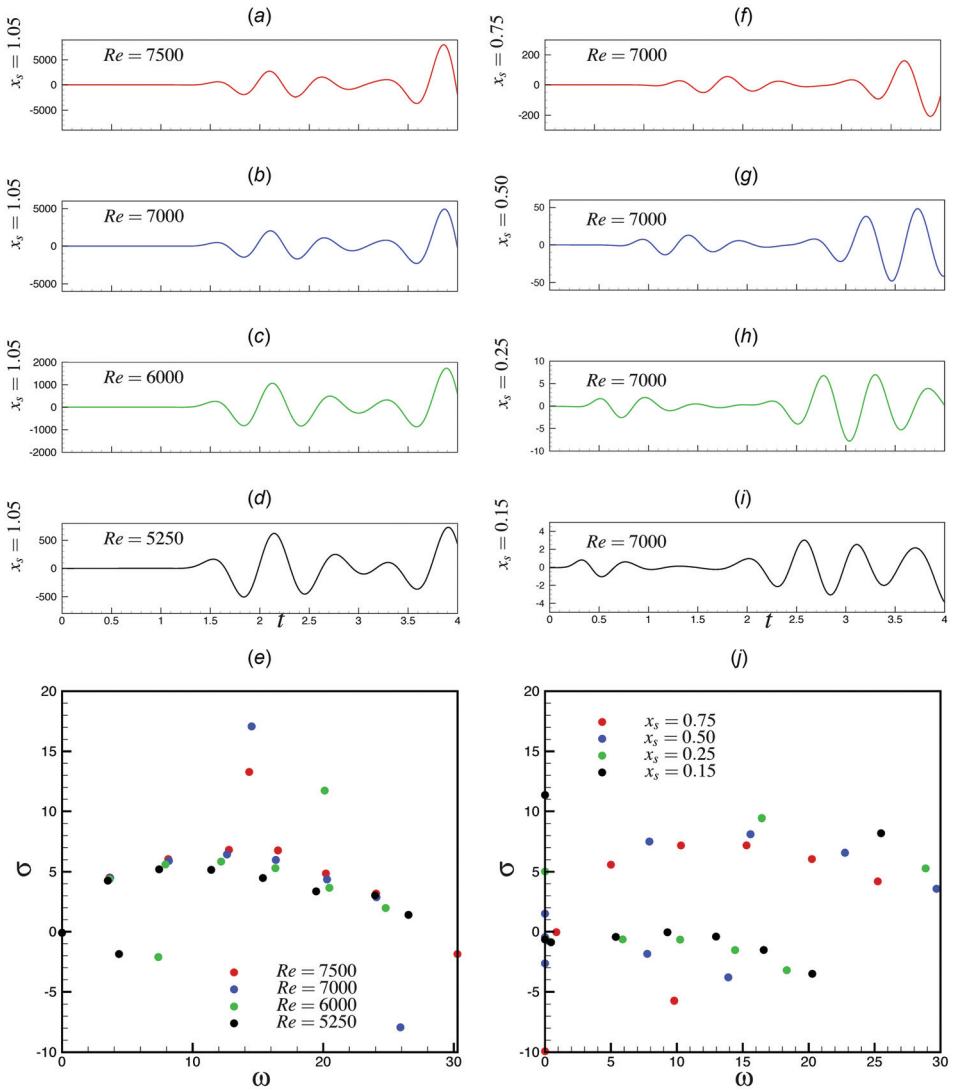

Fig. 18 Impulse responses between *u* and *y*. (*a*)–(*d*) for different Reynolds numbers, the shear-stress sensor being located at $x_s = 1.05$. (*f*)–(*i*) For different locations of the estimation sensor (the Reynolds number being equal to Re = 7000). Zeros of the open-loop transfer function $\overline{T}_{yu}$. (*e*) For different Reynolds numbers, the shear-stress sensor being located at $x_s = 1.05$. (*j*) For different locations of the estimation sensor (the Reynolds number being equal to Re = 7000).

different locations of the estimation sensor in Fig. 18(*j*). In Fig. 18(*e*), we observe a significant number of zeros in the unstable half-plane, independent of the Reynolds number. It reflects the fact that the delay between u and y is constant and large. A different picture emerges from Fig. 18(*j*). For a Reynolds number of Re = 7000, four different locations of the downstream sensor have been evaluated. While the case of $x_s = 0.75$ shows an appreciable number of zeros in the unstable half-plane, moving the sensor closer to the actuator markedly reduces this number. The number of unstable zeros is therefore closely correlated to the delay between the actuator input u and the estimation sensor y. The number of unstable zeros in the plant dynamics is the appropriate quantity to focus on in order to understand the potential failure of the LTR-procedure as the actuator noise is increased ($G/W \ll 1$). We recall that the actuator noise is increased in the LTR-procedure to obtain an ultrafast estimator. Kwakernaak and Sivan [115] have shown that an ultrafast estimator may only be obtained if the transfer function $\overline{T}_{yu}$ has no unstable (right-half-plane) zeros. In actuality, such an ultrafast estimator (if it exists) involves the inverse of the plant dynamics $\overline{T}_{yu}$. The zeros of $\overline{T}_{yu}$ appear as poles in the closed-loop system; for the closed-loop system to be stable, it is therefore required that no unstable zeros exist in $\overline{T}_{yu}$. Hence, the occurrence of unstable zeros in the plant dynamics limits the speed of the Kalman filter as G/W is decreased: Kwakernaak and Sivan [115] have shown that in such a case, the estimation error reaches a constant nonzero value. This constant nonzero estimation error implies that the resulting control signal $u = K\hat{x}$ differs from the full-state control $u = K\bar{x}$. This explains the potential failure of LTR to achieve the favorable robustness properties of the FSC as G/W is decreased. Note that the same argument of existence of unstable zeros in the open-loop transfer function also explains why the performance of an FSC may not achieve perfect (ultrafast) control in the large-gain limit [32].

3.10 Conclusion. We conclude this section by summarizing that closed-loop feedback control of open-cavity flow (and, in general, of oscillator flows) in the SGL can suffer from very small gain and PM that only allow minute deviations from design-conditions before closed-loop stability is lost. Small robustness margins are in particular obtained when strong amplification and large delays exist between the actuator input u and the estimation

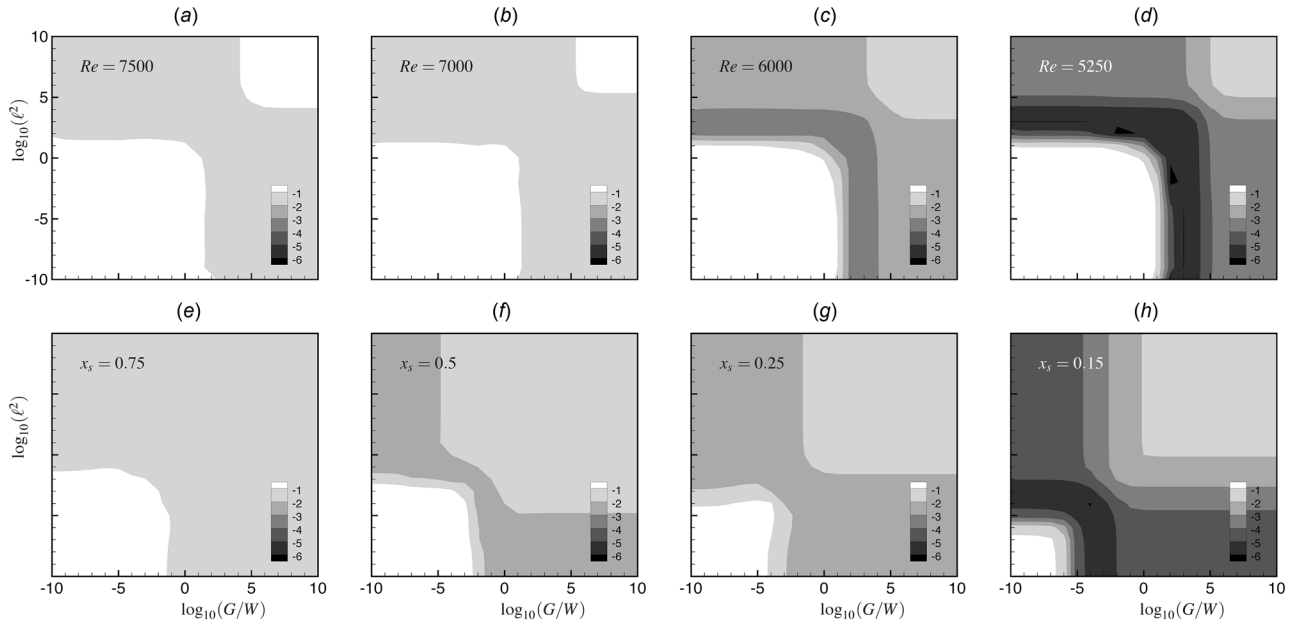

Fig. 19 Gain margin GM^- in the $\log_{10}(G/W)-\log_{10}(\ell^2)$ plane. (*a*)–(*d*) For different Reynolds numbers, the shear-stress sensor being located at $x_s = 1.05$. (*e*)–(*h*) For different locations x_s of the estimation sensor *y*: (*e*) $x_s = 0.75$, (*f*) $x_s = 0.5$, (*g*) $x_s = 0.25$, and (*h*) $x_s = 0.15$. The actuator is located at $x = -0.1$, and the Reynolds number is equal to Re = 7000.

sensor *y*. By artificially increasing the control noise input, we can increase the Kalman gain and force the estimator to react algebraically to the measurement; consequently, we approach a full-state control configuration and benefit from its increased gain and PM. The procedure, known as LTP, shows marked improvements in robustness at the expense of suboptimal performance. Nonetheless, LTP reaches its limits when zeros of the open-loop transfer function exist in the unstable right half-plane. In this case, it is not possible to obtain an ultrafast estimator and the favorable properties of full-state control are lost. We showed that the existence of unstable zeros is linked to the delay between the control input *u* and the estimation sensor *y*. Finally, we considered the $\mathcal{H}_\infty$-control framework that allows us to directly target stability robustness: it was found that the gain and PM could be increased even further compared to LTR results. Such a robustness strategy is effective when designing a single controller that can stabilize base flows over a finite range of Reynolds numbers. Yet, it appears that targeting stability robustness is not sufficient to stabilize the flow field, exhibiting a limit-cycle, far from criticality.

In this above control setup, only one actuator and one sensor have been used, resulting in a single-input-single-output system. Considering a perhaps more realistic configuration with multiple actuators and/or multiple sensors, minor modifications have to be considered at all steps of the control design process; no conceptually different procedure has to be introduced. Model reduction for the stable subspace by balanced truncation is accomplished by an impulse response analysis of the direct problem from *each* actuator and of the adjoint problem from *each* sensor. These responses are gathered into a cross-Gramian matrix that is block-Hankel in nature and where each element consists of a $n_i \times n_o$ matrix (with n_i and n_o as the number of inputs and outputs, respectively). Once the reduction bases have been identified, the control design proceeds as outline above. The multiple input–multiple output (MIMO)-nature of the control setup yields only minor modifications in matrix size (for B_u and C_y) for the Riccati equations. As a further consequence, transfer functions between all the combinations of input and output signals have to be considered and assessed according to the criteria and procedures above.

In particular for three-dimensional flows that are dominated by spanwise-varying instabilities and perturbations, a spanwise distribution of actuators and sensors may be called for to detect three-dimensional structures and to counteract them by actuators.

Related to the choice of the number of actuators/sensors is the decision of where to place them. Performance and robustness measures critically depend on B_u and C_y which govern the type and location of the various input and output elements. For oscillator flows, a perturbation analysis with respect to B_u and C_y would have to be performed and used in an optimization scheme to iteratively determine the optimal (as defined by the user) placement of actuators and sensors. This approach has been taken by Chen and Rowley [116] for a simplified flow model based on the complex Ginzburg–Landau equation. As a substitute for this approach, actuators and sensors are often placed based on state-space properties alone. For the suppression of instabilities in oscillator flows, sensors are placed where the most unstable global mode shows a maximum, assuring an effective sensor signal even in the presence of additive sensor noise. In contrast, the actuator is placed in a region of maximal sensitivity of the instability. In this manner, we promote the notion that a minimal amount of actuation may show great effect on the instability. In other words, actuation is introduced at a location where the instability originates rather than where it has matured to larger amplitudes and would thus require increased control efforts to influence.

4 Control of Noise Amplifiers: Flow Over a Backward-Facing Step

The (low-dimensional) transfer function for the plant and compensator featured prominently in the analysis and design of flow control components for oscillator flows. Nevertheless, a state-space formulation is often the most common representation of the governing equations, involving the state-vector $\mathbf{x}$ of the plant or its estimated equivalent $\hat{\mathbf{x}}$, as well as the system matrices $\mathsf{A}, \mathsf{B}_u, \mathsf{C}_{y,z}$ or their model-reduced analogs.

An alternative approach involves the reformulation of the state-space representation into an input–output system, which abandons the explicit tracking of the state vectors in favor of a direct and explicit mapping between actuator and sensor. This approach is particularly appealing for globally stable flows, known as noise amplifiers, and Sec. 4.1 will introduce and expound the associated techniques. We will use our second generic flow configuration, flow over a backward-facing step (see Fig. 2(*b*)), as a model problem to illustrate this alternative procedure. The backward-facing step configuration is fully described in Hervé et al. [55]; in this

article, we employ the same mesh and boundary conditions. A Poiseuille inflow velocity profile is prescribed on the left boundary of the computational domain. The flow detaches at the step edge and forms a shear layer, which separates the recirculation motion inside the bubble from the external flow. All the quantities are nondimensionalized by the step height and the incoming centerline velocity; the Reynolds number is based on these quantities. The disturbance source B_w and actuator B_u both consist of volume forcings acting on the cross-stream velocity equation, while the estimation sensor C_y and performance sensor C_z both extract shear–stress information from the flow. The exact definitions of these inputs/outputs are given in Hervé et al. [55].

4.1 Formulation as an Input–Output System. We start by stating the formal solution of the governing equations (3*a*)–(3*c*) according to

$$z(t) = \int_0^t \mathsf{C}_z \exp[(t-\tau)\mathsf{A}]\mathsf{B}_u u(\tau)\, d\tau + \int_0^t \mathsf{C}_z \exp[(t-\tau)\mathsf{A}]\mathsf{B}_w w(\tau)\, d\tau + g_z(t) \tag{41}$$

The expression for the measurement signal z is in the form of two memory integrals, for the control input u and the plant noise w, and an additive sensor noise $g_z(t)$ linked to the performance sensor z. The kernels for these memory integrals, i.e., $\mathsf{C}_z \exp[(t-\tau)\mathsf{A}]\mathsf{B}_u$ for the control input and $\mathsf{C}_z \exp[(t-\tau)\mathsf{A}]\mathsf{B}_w$ for the plant noise input, can formally be computed from the system, control, measurement, and plant noise matrices. This approach has been taken in Sec. 3, yielding algebraic matrix equations (such as the Lyapunov equation) that involve these matrices. The quality of the final compensator crucially depends on how accurately these matrices describe the system dynamics (A), the action of the controller (B_u), the response of the sensor (C_z), and the influence of external disturbance sources (B_w). In particular, the effectiveness of the compensator relies on a faithful modeling of the plant noise w via B_w. For oscillator flows, where a strong instability prevails over noise-induced dynamics, the latter modeling problem is less of an issue. For globally stable noise amplifiers, on the other hand, the plant noise w features more prominently in the design process and often becomes the deciding factor between success or failure of the compensated system. The difficulty of obtaining information about the disturbance environment leads us to abandon the concept of a matrix-based approach (for example, it is impossible in an experiment to obtain any information about the forcing B_w).

We therefore propose an alternative that extracts the kernels in Eq. (41) by observing how the system reacts to a user-specified forcing. We thus recast Eq. (41) into

$$z(t) = \int_0^t h_{zu}(t-\tau)u(\tau)\, d\tau + \int_0^t h_{zw}(t-\tau)w(\tau)\, d\tau + g_z(t) \tag{42}$$

and assume the two kernel functions h_{zu} and h_{zw} as unknown functions. It is interesting to note that the functions h_{zu} and h_{zw} can be thought of as the response of the measurement z to an impulsive forcing of the actuator, i.e., $u(t) = \delta(t)$, or an impulsive forcing by noise, i.e., $w(t) = \delta(t)$, in the absence of measurement noise. The Fourier transform (in time) of these impulse responses will produce the corresponding transfer functions T_{zu} and T_{zw}.

Anticipating the use of measured input and output data, we convert to a time-discrete version of Eq. (42)

$$z_n + \sum_{i=1}^{n_a} a_i z_{n-i} = \sum_{j=0}^{n_b} b_j u_{n-j} + \sum_{k=0}^{n_c'} c_k' w_{n-k} + R_n' \tag{43}$$

The performance sensor measurement is given by $z_n = z(n\Delta t_S)$ and equivalently for the other time-dependent variables, with Δt_S as the sampling time. The choice of the sampling time is crucial and will be fully discussed in Sec. 4.2.1. The right-hand side of Eq. (43) can be interpreted as the discrete equivalent of the memory integrals in Eq. (42); the time history of the exogenous inputs u_j and w_k contributes to the measurement signal z_n. The coefficients $\{b_j\}$ and $\{c_k'\}$, weighing the time history for each signal, are assumed unknown. An additional dependence on the history of z has been included in the form of an AR term, also with unknown coefficients $\{a_i\}$. We have truncated all the series $\{a_i\}$, $\{b_j\}$, and $\{c_k'\}$ to n_a, n_b, and n_c' terms. The AR term allows to decrease the total number of unknown coefficients $n_a + n_b + n_c'$ [55]. Yet, this term is not mandatory and may be set removed ($n_a = 0$). The residual term R' contains measurement noise linked to the performance sensor z (note that the AR term in the model may change the color of this noise) and truncation errors.

In physical experiments, information about the disturbance environment w_n is very difficult to come by. For this reason, we replace the disturbance signal w_n by an additional sensor that measures the incoming disturbance environment. This measurement is important for the way in which the actuator reacts to incoming disturbances: the additional sensor is thus placed upstream of the actuator and acts as a proxy for the incoming (noisy) disturbance signal w. By denoting the upstream sensor signal by y_n, we obtain the model

$$z_n + \sum_{i=1}^{n_a} a_i z_{n-i} = \sum_{j=0}^{n_b} b_j u_{n-j} + \sum_{k=0}^{n_c} c_k y_{n-k} + R_n'' \tag{44}$$

where $n_c + 1$ coefficients c_k have been introduced to account for the estimation sensor y. The modified residual vector $\boldsymbol{R}''$ contains the terms involved in $\boldsymbol{R}'$ and additional terms. Indeed, measurement noise in y generates process noise in Eq. (44) and the part of upstream disturbances w which is not observed by y impacts the downstream sensor z as colored (i.e., time-correlated) noise, since noise gets modified according to the transfer functions of the system as it travels from the upstream location of w to the downstream sensor location z. Hence, there are many reasons for R_n'' to be colored noise. This crucial observation has to be explicitly recognized in our current model (44), if we hope to describe the input–output behavior in a physically accurate manner. We therefore replace the residual signal $\boldsymbol{R}''$ by a moving average (MA) signal according to

$$R_n'' \quad \rightarrow \quad R_n + \sum_{p=1}^{n_d} d_p R_{n-p} \tag{45}$$

which, for $d_p \neq 0$, $p = 1, \ldots, n_d$, establishes a correlation between successive instants and thus gives color to the noisy signal $\boldsymbol{R}''$. Our final model describing the relation between inputs u and y and output z is then given as

$$z_n + \sum_{i=1}^{n_a} a_i z_{n-i} = \underbrace{\sum_{j=0}^{n_b} b_j u_{n-j}}_{(1)} + \underbrace{\sum_{k=0}^{n_c} c_k y_{n-k}}_{(2)} + \underbrace{\sum_{p=1}^{n_d} d_p R_{n-p}}_{(4)} + R_n \tag{46}$$

which is referred to as an ARMAX input.

A sketch of the control configuration is shown in Fig. 20, together with the paths of information transfer in the flow. The influence of the control u on z is labeled by Eq. (1), while the influence of the upstream measurement signal y on z is indicated in Eq. (2). Even though the y-signal will capture most of the incoming disturbance (given by path (3) in Fig. 20), it is conceivable that part of the environmental disturbance w will not be detected by the y-sensor upstream, will pass through the fluid system, and impact the measurement z further downstream (see path (4) in Fig. 20) as colored noise. This last pathway is accounted for by the MA part of our ARMAX-model (46).

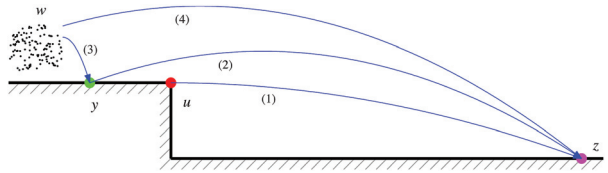

Fig. 20 Sketch indicating the transfer of information to be modeled by the ARMAX structure. Transfer of information (1) from the control *u* to the performance sensor *z*, (2) from the upstream sensor *y* to the performance sensor *z*, (3) the observable part of the disturbance environment *w* measured by *y*, and (4) the part of *w*, unobservable by *y* but impacting the performance sensor *z*.

Setting up the configuration and obtaining learning and validation data sets [55]?
Linux commands:

1. cd Step/BF
2. FreeFem++ newton.edp # compute base-flow
3. cd ../DNSLEARN
4. MATLAB -nodesktop -nosplash < signalgen.m # generate random binary signal
5. FreeFem++-nw dns.edp # launch DNS with previous signal as control input

Even though the model is capable of capturing the principal disturbance dynamics of flow over a backward-facing step in form of an input–output relation, we will make one more adjustment to facilitate the identification of the unknown coefficients $\{a_i\}, \{b_j\}$, and $\{c_k\}$. This adjustment takes advantage of the fact that there is a delay between the inputs at u and y and the resulting output at z; in other words, any response in z must have been caused by a time-delayed input. We thus postulate

$$z_n + \sum_{i=1}^{n_a} a_i z_{n-i} = \sum_{j=\Delta j}^{n_b} b_j u_{n-j} + \sum_{k=\Delta k}^{n_c} c_k y_{n-k} + \sum_{p=1}^{n_d} d_p R_{n-p} + R_n \tag{47}$$

with Δj and Δk denoting the number of time-steps Δt_S for a signal at u or y to first impact the sensor z. The values for Δj and Δk can readily be estimated by a simple time-delay argument based on the base-flow convection speed. The improved formulation (47) avoids the identification of zero-valued coefficients which would result from formulation (46), in other words, we enforce $b_{0..\Delta j-1} = 0$ and $c_{0..\Delta k-1} = 0$.

4.2 System Identification. With the overall structure of the model selected, we force the model by user-specified time-sequences for the input signal u while observing, in the presence of upstream disturbances w, the time-synchronous output signals y and z. For example, we have shown with red solid lines in Figs. 21(*a*)–21(*c*) typical y, u, and z signals that have been measured (y,z) or imposed (u) in our simulation. These data sequences are then used to determine all the coefficients of the selected model structure.

In this section, we will first analyze (Sec. 4.2.1) the spectrum of the various signals and introduce a low-pass filter to focus the learning procedure on the active frequencies contained in the system dynamics and therefore increase the sampling time Δt_S of the model and reduce the number of unknown coefficients $n_a + n_b + n_c - \Delta j - \Delta k + 2$. We will also justify in this section the choice of the control signal $u(t)$ in terms of its amplitude and frequency range. The required complexity of the ARMAX model (reflected in the coefficients $n_a, n_b, n_c, \Delta j$, *and* Δk) will then be discussed (Sec. 4.2.2) and determined by analyzing the autocorrelation function of the signal z and the cross-correlation functions

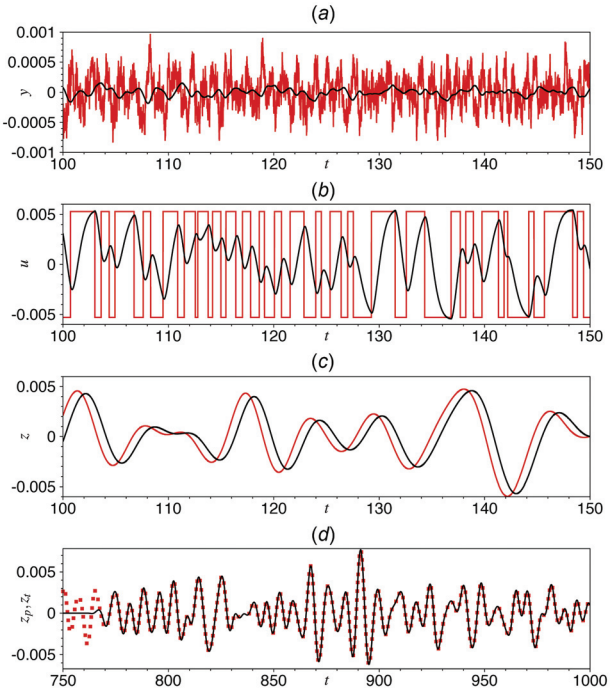

Fig. 21 Learning data set consisting of the recorded measurements from the upstream estimation sensor *y* (*a*), input signal *u* (*b*), and downstream performance sensor *z* (*c*). The validation of the model is shown in (*d*) where the predicted output (solid black line), for a forcing different from the learning set and for a different disturbance environment, is compared to the true signal (red symbols) from the full system. The sensor measurements *y* and *z* and the actuator signal *u* were considered noise-free.

between (u, y) and z. From there, considering a first portion of the simulation dataset (y, u, z) (which will be referred to as the learning dataset in what follows), we can determine (see Sec. 4.2.3) the set of coefficients $\{a\}, \{b\}, \{c\}$, and $\{d\}$ by common least-squares techniques, i.e., the set of coefficients is adjusted to minimize the L_2-error between the true measurement z and the predicted signal given by Eq. (47). After the coefficients have been determined, a second part of the dataset (which will be referred to as the validation data set), different from the learning data set, will be used to assess the generality and fidelity of the identified ARMAX-model.

4.2.1 Sampling Time/Low-Pass Filtering/Learning and Validation Datasets. The spectrum of the clean (noise-free) sensor signal z (in the absence of control, $u = 0$) is shown with a solid red line in Fig. 22(*a*). Frequencies in z are nearly zero above a threshold frequency, $\omega > \omega_c = 2$. In the following, we will therefore focus on the range of frequencies $0 \le \omega \le \omega_c$ and introduce a low-pass filter given by the transfer function

$$T(s) = \frac{\omega_c^2}{s^2 + 2\zeta\omega_c s + \omega_c^2} \tag{48}$$

with $\zeta = 0.8$ (note that $T(0) = 1$ and $T(i\omega_c) = 1/(2i\zeta)$). This filter can be recast into a discrete-in-time state-space form based on the acquisition time of the simulation (in our case, the time step of the DNS, $\Delta t_{\text{DNS}} = 2 \times 10^{-3}$)

$$\begin{pmatrix} \eta_{n+1} \\ \theta_{n+1} \end{pmatrix} = \begin{pmatrix} 1.994 & -0.994 \\ 1 & 0 \end{pmatrix} \begin{pmatrix} \eta_n \\ \theta_n \end{pmatrix} + 0.00391 z_n \tag{49}$$

$$z_n^f = \begin{pmatrix} 0.00205 & 0.00204 \end{pmatrix} \begin{pmatrix} \eta_n \\ \theta_n \end{pmatrix} \tag{50}$$

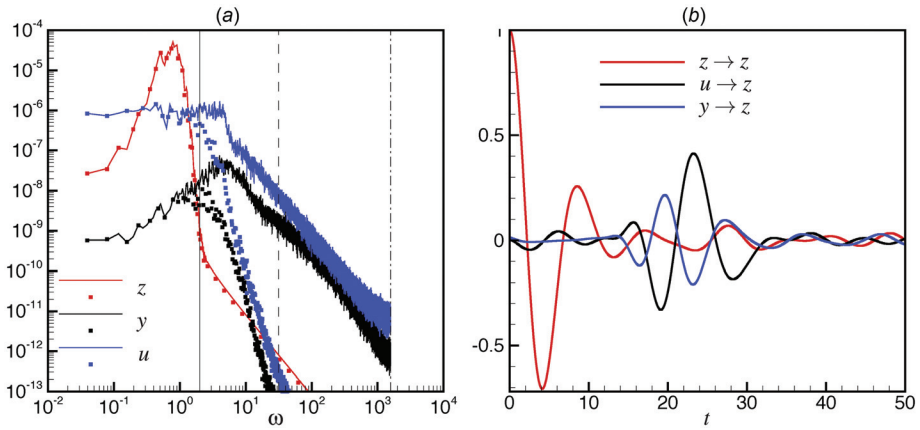

Fig. 22 (*a*) Spectrum magnitude of clean signal *z* (red) and clean signal *y* (black) in simulation without control $u = 0$. The blue lines relate to the chosen *u*-signals. The solid lines correspond to the raw signals and the dotted lines to the filtered ones. The vertical solid line refers to $\omega_c = 2$, the dashed-line to ω_S, and the dashed–dotted line to ω_{DNS}. (*b*) Autocorrelation function of the *z*-signal (red) and cross-correlation functions of the *u* (black) and *y* (blue) signals with the *z*-signal in simulation with control *u*.

Here, z_n is the raw signal, while z_n^f denotes the filtered signal. This state-space form of the filter involves two internal states: η and θ. Within the range of frequencies $0 \leq \omega \leq \omega_c$, this online filter does not modify the amplitude of the signal but introduces a (inconsequential) time-delay of $\Delta t_d = d\arg(T(\omega))/d\omega \approx -0.8$. This is confirmed in Fig. 22(*a*) where the filtered spectrum of z is seen to correspond to the unfiltered one (compare the red-dotted line with the red solid line). In the time domain, shown in Fig. 21(*c*), we observe that the filtered signal (black solid line) corresponds to the unfiltered signal (red solid line) up to a right-shift (without change of shape) with a time delay of Δt_d.

The spectrum of the sensor measurement y is shown with a black solid line in Fig. 22(*a*). Its peak in frequency occurs at $\omega \approx 5$, well above ω_c. Hence, a substantial range of frequencies that are detected by the estimation sensor y is damped by the system as the fluctuations propagate toward the performance sensor z. By applying the low-pass filter given above, the spectrum of the y signal (black-dotted line) is significantly reduced for frequencies above ω_c but unaltered for the lower frequencies (those active at the z-location).

The input signal u has to be chosen sufficiently rich in frequencies over the range $0 \leq \omega \leq \omega_c$ such that all the relevant temporal scales are excited and the pertinent frequency range of the associated transfer function is represented. Also, with a view toward implementation in an experiment, it should be realizable in a concrete, physical setting. A particular signal form that has yielded encouraging results in a variety of system identification tasks is the random binary signal, representing square waves of random duration or duty cycles. This signal form excites a very broad range of frequencies and is readily feasible in an experiment—thus satisfies our requirements for an efficient identification process. In what follows, we choose a signal u that covers the frequency range $0 \leq \omega \leq 5$, i.e., all relevant frequencies in z. The amplitude of the signal u was chosen such that the variance of the filtered z-signal (in the presence of upstream disturbances w and control u) is doubled compared to the unforced case ($u = 0$). This criterion was met in our case by choosing values for the square waves equal to $u = \pm 0.0054$. The unfiltered (red line) and filtered (black line) signals are shown in the time-domain in Fig. 21(*b*). We note that damping the frequencies above $\omega_c = 2$ strongly modifies the signal. As before, we observe a characteristic time-delay between the two signals. The spectra of the unfiltered and filtered u signals are shown, using blue solid and dotted lines, in Fig. 22(*a*).

The sampling time Δt_S has to be chosen judiciously. On the one hand, it should be sufficiently small to ensure no energy at the Nyquist-frequency $\omega_S = \pi/\Delta t_S$ in all the filtered signals. On the other hand, it should be as large as possible to reduce the number of samples, avoid redundancies in the signal and facilitate the identification process. Here, we chose $\Delta t_S = 0.1$, which yields a Nyquist frequency of $\omega_S = 31.4$, i.e., an order of magnitude higher than the cut-off frequency $\omega_c = 2$.

4.2.2 Determination of Parameters n_a, n_b, n_c, Δj, and Δk in ARMAX Model. A robust and effective model should accurately predict the output signal z, even though the input signal and/or disturbance environment has not been part of the identification process (learning dataset). Balancing the model's complexity and the size of the learning samples is a nontrivial task. Learning data sets that are short compared to the model's complexity will yield small errors during the identification process, but will result in rather large errors when validated on a distinct validation data set. This phenomenon is referred to as over-learning which has to be avoided; instead, a balance between the errors from the learning and testing data set has to be attempted [117].

To determine the required complexity of the model, we have to specify the number of coefficients to identify in the respective summations in Eq. (47) and therefore determine the values of the coefficients $n_a, n_b, n_c, n_d, \Delta j$, and Δk. The coefficient n_a quantifies the degree of memory in the measurement signal z. It can straightforwardly be related to the autocorrelation length of the signal z, which may be deduced from inspection of the autocorrelation function $C(k) = \langle z_n z_{n-k} \rangle$ of the measurement signal z. The autocorrelation function $C(k)/C(0)$ is presented in Fig. 22(*b*) with a red-solid line: the correlation time of the signal z is $t \approx 2$, which translates to $n_a = 20$.

The coefficients Δj, Δk, n_b, and n_c may be determined from the cross-correlation functions $\langle u_n z_{n-k} \rangle$ and $\langle y_n z_{n-k} \rangle$. These cross-correlation functions represented in Fig. 22(*b*) by black and blue lines are related to the impulse responses from u and y to z. Hence, the delays Δj and Δk may readily be estimated from these curves. Here, we chose $\Delta j = \Delta k = 101$, which corresponds to a delay of about ten time-units. In the case where no AR part is chosen ($n_a = 0$), the sequences $\{b_j\}$ and $\{c_k\}$ represent the impulse responses from u and y to z. In this case, $n_b \Delta t_S$ and $n_c \Delta t_S$ should roughly correspond to the cross-correlation lengths shown in Fig. 22(*b*). In the case $n_a = 0$, we chose $n_b = n_c = 400$, which corresponds to a time of about 40 time-units for the impulse responses to vanish. In the case $n_a \neq 0$, n_b and n_c will be smaller: for $n_a = 20$, we chose $n_b = n_c = 160$. Finally, the coefficient n_d measuring the amount of memory in the noise, that directly impacts z, must be determined empirically. The number of terms depends on

the presence or absence of noise in y, z, or u, the color of these noise components, the presence or absence of disturbance sources that are not visible by y, etc.

4.2.3 Determination of a_i, b_j, and c_k in the ARMAX Model and Subsequent Model Validation. We consider the filtered signals y, u, and z of the learning dataset shown with black lines in Figs. 21(*a*)–21(*c*). These signals have been sampled at $\Delta t_S = 0.1$ over the time-range $50 \leq t \leq 750$. We then chose $n_a = 0$, $(\Delta j = 101, n_b = 400)$, $(\Delta k = 101, n_c = 400)$, and $n_d = 0$ for the model structure, and the coefficient sets $\{a\}, \{b\}, \{c\}, \{d\}$ have been obtained by least-squares techniques (*armax* function in MATLAB). In a subsequent step, the identified model is validated by subjecting it to a forcing signal u and disturbance environment w that have not been part of the learning data set during the identification phase. In particular, we compare the predicted model output z_p for the downstream sensor to the true filtered output z_t from the direct numerical simulation over $750 \leq t \leq 1000$; this comparison is shown in Fig. 21(*d*), and we may quantity the quality of the model by evaluating the relative error $\mathrm{ERR}_v = ||z_p - z_t||_2/||z_t||_2 = 0.007$. After an initial transient period—approximately given by the travel time of a perturbation from the sensor y or actuator u to the downstream sensor z—the model-predicted and true measurement signals coincide, indicating that the identified model is capable of predicting the performance measure z from the two input signals y and u. The identified impulse responses h_{zu} and h_{zy} are represented in Fig. 23(*a*) with a solid black and a solid red line. We observe a time-delay of around 12 time-units between (u, y) and z.

For sake of completeness, we have given in Tables 2 and 3, the model-error ERR_v with one (y) or two (y, u) inputs for different values of the model structure coefficients. We have also assessed the influence of noise which may corrupt the measurement sensors y and z and the effect of the filtering procedure.

4.3 Control Design by Disturbance Rejection. After the coefficients of the ARMAX model have been determined and the performance and accuracy of the model have been verified, a compensator can be designed. The predictive nature of the model, i.e., given the incoming signal y, the response in z can be computed, suggests a control design based on disturbance rejection ideas. The underlying principle of this concept centers around the design of a control signal u, such that its response in z destructively interferes with the response in z induced by the incoming perturbation (measured by y). Mathematically, the signal z from the downstream sensor contains two sources: the user-defined control u and the measured upstream sensor y, which, in terms of transfer functions, can be written as $z = \mathsf{T}_{zy} y + \mathsf{T}_{zu} u$. The goal then is to minimize the signal z, for which we put forward the objective $z = 0$. The control law then follows immediately as $u = -\mathsf{T}_{zu}^{-1}\mathsf{T}_{zy} y$: given the upstream sensor measurements y, this latter expression

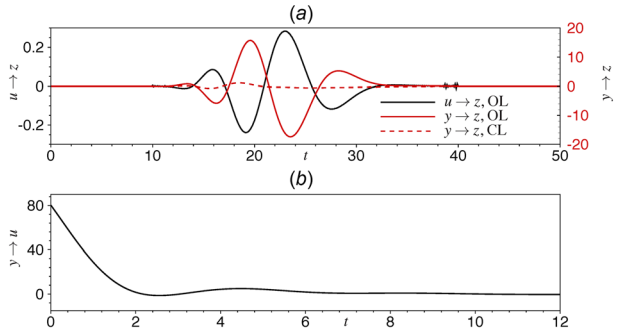

Fig. 23 Impulse responses (*a*) from *u* to *z* in open-loop (black solid line), from *y* to *z* in open-loop (red solid-line) and from *y* to *z* in closed-loop (dashed-red line). The impulse response of the control law from *y* to *u* is shown in (*b*).

Table 2 Model performance ERR_v with one (y) output for different model structure coefficients. A noise level of 25% means that the standard deviation of the added filtered white noise is equal to 0.25 times the standard deviation of the filtered noise-free signal. $\mathrm{ERR}_v = ||z_p - z_t||_2/||z_t||_2$ is evaluated on filtered noise-free data sets.

Inputs	Noise y (%)	Noise z (%)	Filtering	n_a	$(\Delta j, n_b)$	$(\Delta k, n_c)$	n_d	ERR_v(%)
Effect of noise on y and z with $n_a = 0$								
y	0	0	Y	0	(101, 400)		0	1
y	25	0	Y	0	(101, 400)		0	17
y	50	0	Y	0	(101, 400)		0	39
y	0	25	Y	0	(101, 400)		0	7
y	0	50	Y	0	(101, 400)		0	14
Effect of noise on y and z with $n_a = 20$								
y	0	0	Y	20	(101, 160)		0	15
y	25	0	Y	20	(101, 160)		0	24
y	0	25	Y	20	(101, 160)		0	61
Effect of n_d with noise-free sensors and $n_a = 20$								
y	0	0	Y	20	(101, 160)		0	15
y	0	0	Y	20	(101, 160)		5	7
y	0	0	Y	20	(101, 160)		10	1
Effect of n_d with noisy y and noise-free z and $n_a = 20$								
y	25	0	Y	20	(101, 160)		0	24
y	25	0	Y	20	(101, 160)		5	19
y	25	0	Y	20	(101, 160)		10	21
Effect of n_d with noise-free y and noisy z and $n_a = 20$								
y	0	25	Y	20	(101, 160)		0	61
y	0	25	Y	20	(101, 160)		5	55
y	0	25	Y	20	(101, 160)		10	42
y	0	25	Y	20	(101, 160)		15	24
y	0	25	Y	20	(101, 160)		20	20
y	0	25	Y	20	(101, 160)		25	15
y	0	25	Y	20	(101, 160)		30	14
Effect of filtering								
y	0	0	N	0	(101, 400)		0	33
y	25	0	N	0	(101, 400)		0	91
y	0	25	N	0	(101, 400)		0	52
y	0	0	N	20	(101, 400)		0	40
y	25	0	N	20	(101, 400)		0	87
y	0	25	N	20	(101, 400)		0	100

Table 3 Model performance ERR_v with two (u, y) outputs for different model structure coefficients. A noise level of 25% means that the standard deviation of the added filtered white noise is equal to 0.25 times the standard deviation of the filtered noise-free signal. $\mathrm{ERR}_v = ||z_p - z_t||_2/||z_t||_2$ is evaluated on filtered noise-free data sets.

Inputs	Noise y (%)	Noise z (%)	Filtering	n_a	$(\Delta j, n_b)$	$(\Delta k, n_c)$	n_d	ERR_v(%)
Effect of noise with $n_a = 0$								
(y,u)	0	0	Y	0	(101, 400)	(101, 400)	0	1
(y,u)	25	0	Y	0	(101, 400)	(101, 400)	0	24
(y,u)	0	25	Y	0	(101, 400)	(101, 400)	0	8
Effect of noise with $n_a = 20$								
(y,u)	0	0	Y	20	(101, 160)	(101, 160)	1	5
(y,u)	25	0	Y	20	(101, 160)	(101, 160)	1	25
(y,u)	0	25	Y	20	(101, 160)	(101, 160)	25	8

for u accomplishes a vanishing downstream signal z. The inversion of the control-to-sensor transfer function T_{zu} requires special care, as it is conceivable (and often the case) that the transfer function is small or zero for certain frequencies. For these frequencies, the inversion would fail or yield undesirable large control gains. This ill-conditioning can be avoided, however, by applying a pseudo-inversion instead of an exact inversion. This

regularization step allows us to specify a lower threshold below which no control action is taken and consequently yields an effective control strategy.

Alternatively, the control strategy can also be designed in the time-domain rather than the frequency-domain. It is the fact that u is located downstream of y (in principle $\Delta j < \Delta k$), which ensures that the resulting control law is well-defined and stable: u_n may indeed explicitly be expressed as a function of past values of $u_{j<n}$ and past values of $y_{k<n}$. A more tunable control law may be obtained by considering a regularized inversion of a state-space formulation expressing the fact that the z signal should be minimal over a specified time-horizon. The impulse response of the resulting control law is displayed in Fig. 23(*b*). In a closed-loop configuration, this control law manages to nearly suppress the amplification phenomena between y and z, as shown by the red-dashed line in Fig. 23(*a*).

How to obtain a controller by pseudo-inversion and launch a DNS with this controller [55]?
Linux commands:

1. cd ../Reg
2. MATLAB -nodesktop -nosplash < modelinv.m # design controller by pseudo-inversion of the system
3. cd ../DNSCONTROL
4. FreeFem++-nw dns.edp # launch DNS with control law determined above

Comments. For an arbitrary discrete-time control horizon T, the output measurement vector Z_T that results from a combination of a future control vector U^f, a past control vector U^p, and a past measurement vector Y^p reads

$$\underbrace{\begin{pmatrix} z_n \\ z_{n+1} \\ \vdots \\ z_{n+T} \end{pmatrix}}_{\mathsf{Z}_T} = \underbrace{\begin{pmatrix} h_0^u & & & \\ h_1^u & h_0^u & & \\ \vdots & & \ddots & \\ h_T^u & \dots & \dots & h_0^u \end{pmatrix}}_{\mathsf{H}_u} \underbrace{\begin{pmatrix} u_n \\ u_{n+1} \\ \vdots \\ u_{n+T} \end{pmatrix}}_{\mathsf{U}^f} + \underbrace{\begin{pmatrix} h_1^u & \dots & h_{T-1}^u & h_T^u \\ h_2^u & \dots & h_T^u & 0 \\ \vdots & \iddots & 0 & \vdots \\ h_T^u & 0 & 0 & 0 \\ 0 & \dots & 0 & 0 \end{pmatrix}}_{\mathsf{G}_u} \underbrace{\begin{pmatrix} u_{n-1} \\ u_{n-2} \\ \vdots \\ u_{n-T} \end{pmatrix}}_{\mathsf{U}^p} \mathsf{Y}^p + \underbrace{\begin{pmatrix} h_0^y & \dots & h_{T-1}^y & h_T^y \\ h_2^y & \dots & h_T^y & 0 \\ \vdots & \iddots & 0 & \vdots \\ h_T^y & 0 & 0 & 0 \end{pmatrix}}_{\mathsf{G}_y} \begin{pmatrix} y_n \\ y_{n-1} \\ \vdots \\ y_{n-T} \end{pmatrix} \tag{51}$$

The sequences h_i^u and h_i^y are the Markov parameters of the impulse responses from u and y to z

$$z_n = \sum_{i=0} h_i^u u_{n-i} + \sum_{i=0} h_i^y y_{n-i} \tag{52}$$

These parameters may straightforwardly be obtained once the ARMAX model has been identified (code Step/Reg/modelinv.m). Supplemental material is available under the "Supplemental Data" tab on the ASME Digital Collection. By minimizing $||\mathsf{Z}_T||^2$, the compensator is finally obtained via

$$\mathsf{U}^f = (-\mathsf{H}_u^+ \mathsf{G}_u)\mathsf{U}^p + (-\mathsf{H}_u^+ \mathsf{G}_y)\mathsf{Y}^p \tag{53a}$$

$$u_n = (\,1 \quad 0\dots \quad 0\,)\mathsf{U}^f \tag{53b}$$

where H_u^+ refers to the Moore–Penrose pseudo-inverse.

4.4 Control Performance. After the compensator, given by the control law $u = -\mathsf{T}_{zu}^{-1}\mathsf{T}_{zy}y$, has been designed, we can now apply it to the direct numerical simulations and address performance issues associated with the application of a reduced-order compensator to a high-dimensional flow configuration. To this end, the control law from y to u is recast in a state-space form and resampled at the acquisition rate (in our case, with the time-step of the simulation $\Delta t_{\mathrm{DNS}} = 2 \times 10^{-3}$) using bilinear interpolation. The spectra, in magnitude and phase, of the original (red line) and resampled (black line) control are depicted in Figs. 24(*a*) and 24(*b*). The raw signal y is directly fed into the controller without filtering, which avoids time-delays. Note that all the high frequencies in the signal y ($\omega > \omega_c$) are efficiently damped by the controller, since the controller acts as a low-pass filter (see Fig. 24(*a*)). The resulting control signal u is applied to the numerical simulations and the response z at the downstream sensor is recorded. For an effective control effort, we should expect a noticeable reduction in the downstream measurement signal z, when compared to the uncontrolled ($u = 0$) case, since such a reduction has been the explicit objective of the control design.

The control is switched on at time $t = 1000$. The control law u and the performance signal z are presented as a function of time in Figs. 25(*a*) and 25(*b*). We observe a significant reduction in the amplitude of the performance sensor: we find that the standard deviation of the z-signal is 0.0017 without control and 0.00018 with applied control. This should be compared to the values obtained from the reduced-order models, where we expect 0.0016 without control and 0.00012 with applied control. This shows that the designed control laws are sufficiently robust to account for the discrepancies between the modeled transfer functions and the actual ones (those in the numerical simulation). The performance in the DNS when updating the control law every $\Delta t_S = 0.1$ (while keeping the acquisition time of the control law fixed at Δt_{DNS}) is 0.00022, which is just slightly above the optimal value of 0.00018. When the acquisition time of the control law is set to $\Delta t_S = 0.1$, the performance is worse and equal to 0.0012, better than the uncontrolled performance (0.0017) but far worse than the previous controlled simulations. It seems also interesting to quantify the reduction of total perturbation energy of the fluid system to assess whether our control efforts reach beyond the strict limits of the control objective. Even though some reduction of local perturbation energy may be anticipated in the vicinity of the downstream sensor, its specific amount and spatial extent are flow-dependent and need to be evaluated for each case. The results from the uncontrolled and controlled simulations are displayed in Fig. 25(*c*). We observe a remarkable reduction of the total perturbation energy, with approximately 2 orders of magnitude between the uncontrolled and controlled case. This reduction concerns the perturbation energy integrated over the entire computational domain.

The transfer function T_{yu} is approximately zero since the actuator u is located downstream of the estimation sensor y. For this reason, the closed loop cannot become unstable (see Sec. 3.3). Hence, there is no necessity to address stability-robustness issues here; only performance-robustness issues are of concern and have briefly been discussed in the last paragraph. Note that Belson et al. [53] argued that feedback configurations in such convective flows could nonetheless have better performance-robustness properties than the present feed-forward setup in the case where new noise sources appear after control design.

4.5 Conclusion. We have presented an effective way to account for the unknown upstream disturbance w which drives the dynamics of amplifier flows. For this, we introduced an upstream sensor y which is in charge of estimating the incoming perturbations. The reduced-order model has therefore two inputs, the upstream measurement y and actuator law u, and one output, the downstream measurement z. Once the model-structure has been chosen by inspection of the autocorrelation function of z and the cross-correlation functions between (y, u) and z, the model

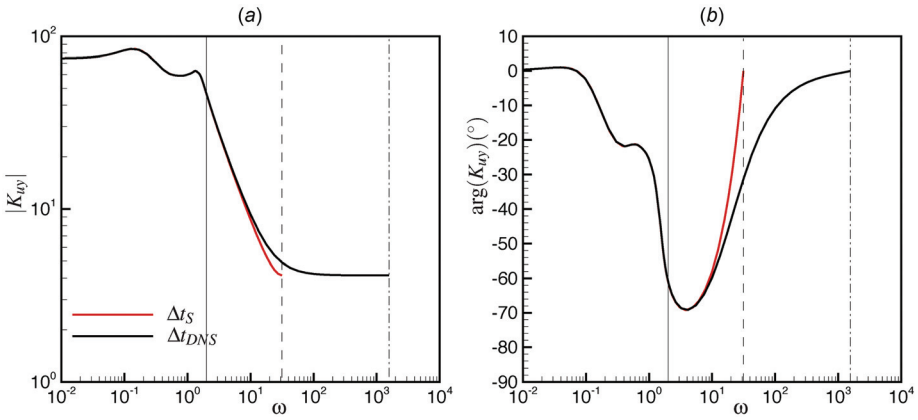

Fig. 24 Magnitude (*a*) and phase (*b*) of the control law between *y* and *u*. The red line refers to the (original) control law obtained for the sampling time $\Delta t_S = 0.1$, while the black line corresponds to the resampled law (bilinear transform) at the DNS time step $\Delta t_{DNS} = 2\times10^{-3}$. The vertical solid line refers to $\omega_c = 2$, the dashed line to ω_S, and the dashed–dotted line to ω_{DNS}. Note that the controller is also used to filter the high frequencies present in the *y* signal, which justifies that the control law must be resampled with respect to the acquisition time Δt_{DNS}.

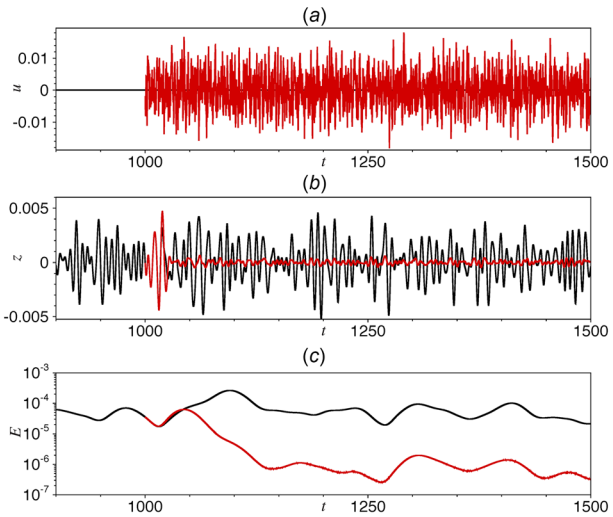

Fig. 25 (*a*) Control signal *u*(*t*) versus time. (*b*) Performance sensor *z*(*t*). (*c*) Global perturbation energy *E*(*t*). In all the plots, the black (respectively, red) line represents the uncontrolled (respectively, controlled) case.

coefficients are obtained by fitting the model to measured input–output data. The control law may then straightforwardly be obtained by inversion of the transfer-function between u and z. The obtained control law is effective both when applied on the reduced-order model (for which it was devised) and when applied to the large-scale simulation (with only a small loss in performance).

Owing to the missing or negligible feedback from the downstream actuator to the upstream sensor, control setups for feedforward configurations are less prone to robustness issues; in fact, stability-robustness is guaranteed in this case, while performance-robustness has to be assessed from case to case. This feature has also been observed for the flow over the backward-facing step: a remarkable level of performance-robustness has been found, as the disturbance levels have been increased far beyond the conditions used in the system-identification step. Disturbances that are not seen by the upstream sensor y [55], or measurement noise corrupting (y, z), and actuator noise u shows up as colored noise in the reduced-order model. Such noise may be accounted for by the moving-average part in this model. The same type of robustness to Reynolds number changes, however, has been less pronounced; this can be associated with the fact that even moderate variations in the Reynolds number can imply substantial changes in the linear flow behavior, as illustrated in Fig. 13 comparing transfer functions for two relatively close Reynolds numbers. As mentioned above, a feedback configuration, as proposed in Ref. [53], may produce superior results.

Adaptive control is an alternative robustification approach: rather than operating the controller with optimal, but fixed coefficients, adaptive controllers adjust the coefficients according to a fed-back downstream performance signal. Promising results have been obtained using this technique (see Ref. [29]); quantitative robustness measures or performance bounds, however, are difficult to come by. For our specific application to flow over a backward-facing step, adaptation (or re-acquisition of the ARMAX model coefficients) was unnecessary due to the good robustness properties of the underlying ARMAX filter. In other flow situations, where this is not the case, adaptation may provide an effective and elegant solution.

5 Outlook

Application of the presented techniques in experimental situations is possible, and different strategies may be followed.

In the case of oscillator flows, choosing a reduced-order model obtained by Galerkin projection stipulates that the numerical simulation be as close as possible to the experimental situation. To guarantee the success of the compensator (designed using a large-scale numerical simulation) in the experiment, a robust control law is mandatory. Decoupling the dynamics between the estimator and the controller by pushing the gains generally improves the robustness of the compensator. Yet, the presence of unstable zeros in the open-loop transfer function (due to delays) may lead to failure. The use of $\mathcal{H}_\infty$-control then allowed us to design a controller with even better stability robustness properties, by minimizing the infinity-norm of the closed-loop system between actuator noise and control signal. We have seen in this article that increasing stability–robustness characteristics may easily extend the operating-range (in terms of Reynolds number, for example) of a control law. However, coping with nonlinearities, which are triggered, if the control is switched on while the system is in a limit-cycle, seems to be far more difficult. To overcome this difficulty, nonlinear models accounting for finite-amplitude perturbations about a fixed-point may be required. Encouraging results in this direction have recently been obtained using (and extending) the POD-DEIM technique [83,84], which produces nonlinear reduced-order models based on distinct bases that represent the

unstable linear processes as well as the saturating nonlinear terms. Another research direction concentrates on avoiding a large-scale numerical model by solely using input–output data and system identification techniques. If a controller that manages to stabilize the unstable system is available (this is a strong requirement, and the objective in this case is simply to design a better controller that is, for example, more efficient or more robust), it is possible to identify the unstable open-loop transfer function directly in the experiment [60]. If this approach fails, it is also possible, in principle, to identity nonlinear polynomial models such as nonlinear autoregressive exogenous (NLARX) models or neural nets [117]. Yet, first attempts in this direction have shown that such models are extremely sensitive.

In the case of amplifier flows, the presented strategy to obtain reduced-order models only relies on input–output data, and the resulting control laws appear robust. Experimental applications of similar strategies have already been attempted [9,21]. Difficulties remain for handling perturbations which are three-dimensional (in principle, arrays of sensors and actuators aligned in the spanwise direction should solve this problem, but the dimensions of the model structures become increasingly important) or of finite amplitude in the case when the upstream disturbance environment is not sufficiently weak. The latter point in fact requires us to consider nonlinear models for the identification process, such as NLARX models. Finally, introducing performance-robustness in the objective functional would be of great help and the method of choice to extend the range of operating conditions. Alternative strategies such as adaptive control may also be attempted in this respect [29].

Applications of flow control methodology to experiments are dominated by a data-based approach using system-identification techniques (see, e.g., Refs. [8,10]). A range of methods, such as ERA, OKID, or subspace identification techniques, have been applied, and nonlinear generalizations and extensions of system identification have been explored as well [82]. The use of data-based techniques to describe prestabilized systems [60,61] or systems in limit-cycle behavior [4] has shown encouraging and robust results; less success has been achieved by model-based Galerkin projections [17] applied to experimental situations. The concept of a dynamical observer has been explored as a data-driven methodology to identify and control a flow [50]; this single-input multiple-output (consisting of the POD-coefficients of a reduced-order model) technique has yielded promising results and is currently being implemented in an experimental setting.

Nomenclature

A = system matrix
B = control matrix
C = measurement matrix
g = measurement noise
G = measurement noise covariance
GM^{+} = positive gain margin
GM^{-} = negative gain margin
J = estimator system matrix
K = control gain
ℓ = control cost parameter
L = Kalman gain
T_{xy} = transfer function from y to x
w = plant noise/control noise
W = control noise covariance
$\mathbf{x}$ = state vector
y = estimation sensor
z = performance sensor
Overbars denote *model-reduced* quantities. Hats indicate *estimated* quantities.

References

[1] Bewley, T., 2001, "Flow Control: New Challenges for a New Renaissance," Prog. Aerosp. Sci., **37**(1), pp. 21–58.
[2] Collis, S., Joslin, R., Seifert, A., and Theofilis, V., 2004, "Issues in Active Flow Control: Theory, Control, Simulation, and Experiment," Prog. Aerosp. Sci., **40**(4), pp. 237–289.
[3] Kim, J., and Bewley, T., 2007, "A Linear Systems Approach to Flow Control," Ann. Rev. Fluid Mech., **39**(1), pp. 383–417.
[4] Cattafesta, L., Song, Q., Williams, D., Rowley, C., and Alvi, F., 2008, "Active Control of Flow-Induced Cavity Oscillations," Prog. Aerosp. Sci., **44**(7), pp. 479–502.
[5] Sipp, D., Marquet, O., Meliga, P., and Barbagallo, A., 2010, "Dynamics and Control of Global Instabilities in Open-Flows: A Linearized Approach," ASME Appl. Mech. Rev., **63**(3), p. 030801.
[6] Brunton, S., and Noack, B., 2015, "Closed-Loop Turbulence Control: Progress and Challenges," ASME Appl. Mech. Rev., **67**(5), p. 050801.
[7] Gad-el Hak, M., 2001, *The MEMS Handbook*, CRC Press, Boca Raton, FL.
[8] Rathnasingham, R., and Breuer, K., 2003, "Active Control of Turbulent Boundary Layers," J. Fluid Mech., **495**, pp. 209–233.
[9] Erdmann, R., Pätzold, A., Engert, M., Peltzer, I., and Nitsche, W., 2011, "On Active Control of Laminar–Turbulent Transition on Two-Dimensional Wings," Philos. Trans. R. Soc. London A, **369**(1940), pp. 1382–1395.
[10] Juillet, F., McKeon, B., and Schmid, P., 2014, "Experimental Control of Natural Perturbations in Channel Flow," J. Fluid Mech., **752**, pp. 296–309.
[11] Cattafesta, L., Garg, S., Choudhari, M., and Li, F., 1997, "Active Control of Flow Induced Cavity Resonance," AIAA Paper No. 97-1804.
[12] Mongeau, L., Kook, H., and Franchek, M., 1998, "Active Control of Flow-Induced Cavity Resonance," AIAA/CEAS Paper No. 98-2349.
[13] Williams, D., and Morrow, J., 2001, "Adaptive Control of Multiple Acoustic Modes in Cavities," AIAA Paper No. 2001-2769.
[14] Williams, D., Rowley, C., Colonius, T., Murray, R., MacMartin, D., Fabris, D., and Albertson, J., 2002, "Model-Based Control of Cavity Oscillations. Part I: Experiments," AIAA Paper No. 2002-0971.
[15] Kegerise, M., Cattafesta, L., and Ha, C., 2002, "Adaptive Identification and Control of Flow-Induced Cavity Oscillations," AIAA Paper No. 2002-3158.
[16] Cabell, R., Kegerise, M., Cox, D., and Gibbs, G., 2006, "Experimental Feedback Control of Flow-Induced Cavity Tones," AIAA J., **44**(8), pp. 1807–1816.
[17] Samimy, M., Debiasi, M., Caraballo, E., Serrani, A., Yuan, X., Little, J., and Myatt, J., 2007, "Feedback Control of Subsonic Cavity Flows Using Reduced-Order Models," J. Fluid Mech., **579**, pp. 315–346.
[18] Becker, R., Garwon, M., Guknecht, C., Barwolff, G., and King, R., 2005, "Robust Control of Separated Shear Flows in Simulation and Experiment," J Process Control, **15**(6), pp. 691–700.
[19] Henning, L., and King, R., 2007, "Robust Multivariable Closed-Loop Control of a Turbulent Backward-Facing Step Flow," J. Aircr., **44**(1), pp. 201–208.
[20] Pastoor, M., Henning, L., Noack, B., King, R., and Tadmor, G., 2008, "Feedback Shear Layer Control for Bluff Body Drag Reduction," J. Fluid Mech., **608**, pp. 161–196.
[21] Gautier, N., and Aider, J.-L., 2014, "Feed-Forward Control of a Perturbed Backward-Facing Step Flow," J. Fluid Mech., **759**, pp. 181–196.
[22] Gautier, N., Aider, J.-L., Duriez, T., Noack, B., Segond, M., and Abel, M., 2015, "Closed-Loop Separation Control Using Machine Learning," J. Fluid Mech., **770**, pp. 442–457.
[23] Gharib, M., 1987, "Response of the Cavity Shear Layer Oscillations to External Forcing," AIAA J., **25**(1), pp. 43–47.
[24] Roussopoulos, K., and Monkewitz, P., 1996, "Nonlinear Modelling of Vortex Shedding Control in Cylinder Wakes," Physica D, **97**(1), pp. 264–273.
[25] Illingworth, S., Naito, H., and Fukagata, K., 2014, "Active Control of Vortex Shedding: An Explanation of the Gain Window," Phys. Rev. E, **90**(4), p. 043014.
[26] Yan, P., Debiasi, M., Yuan, X., Little, J., Ozbay, H., and Samimy, M., 2006, "Experimental Study of Linear Closed-Loop Control of Subsonic Cavity Flow," AIAA J., **44**(5), pp. 929–938.
[27] Kestens, T., and Nicoud, F., 1998, "Active Control of an Unsteady Flow Over a Rectangular Cavity," AIAA Paper No. 98-2348.
[28] Fabbiane, N., Semeraro, O., Bagheri, S., and Henningson, D., 2014, "Adaptive and Model-Based Control Theory Applied to Convectively Unstable Flows," ASME Appl. Mech. Rev., **66**(6), p. 060801.
[29] Fabbiane, N., Simon, B., Fischer, F., Grundmann, S., Bagheri, S., and Henningson, D., 2015, "On the Role of Adaptivity for Robust Laminar Flow Control," J. Fluid Mech., **767**, pp. R1–R2.
[30] Gunzburger, M., 2003, *Perspectives in Flow Control and Optimization*, Vol. 5, SIAM, Philadelphia, PA.
[31] Skogestad, S., and Postlethwaite, I., 2007, *Multivariable Feedback Control: Analysis and Design*, Vol. 2, Wiley, New York.
[32] Joshi, S., Speyer, J., and Kim, J., 1997, "A Systems Theory Approach to the Feedback Stabilization of Infinitesimal and Finite-Amplitude Disturbances in Plane Poiseuille Flow," J. Fluid Mech., **332**, pp. 157–184.
[33] Bewley, T., and Liu, S., 1998, "Optimal and Robust Control and Estimation of Linear Paths to Transition," J. Fluid Mech., **365**, pp. 305–349.
[34] Cortelezzi, L., Speyer, J., Lee, K., and Kim, J., 1998, "Robust Reduced-Order Control of Turbulent Channel Flows Via Distributed Sensors and Actuators," 37th IEEE Conference on Decision and Control (CDC), Tampa, FL, Dec. 16–18, Vol. 2, pp. 1906–1911.
[35] Lee, K., Cortelezzi, L., Kim, J., and Speyer, J., 2001, "Application of Reduced-Order Controller to Turbulent Flows for Drag Reduction," Phys. Fluids, **13**(5), pp. 1321–1330.
[36] Lauga, E., and Bewley, T., 2004, "Performance of a Linear Robust Control Strategy on a Nonlinear Model of Spatially Developing Flows," J. Fluid Mech., **512**, pp. 343–374.

[37] Gavarini, M., Bottaro, A., and Nieuwstadt, F., 2005, "Optimal and Robust Control of Streaks in Pipe Flow," J. Fluid Mech., **537**, pp. 187–219.
[38] Laub, A., Heath, M., Paige, C., and Ward, R., 1987, "Computation of System Balancing Transformations and Other Applications of Simultaneous Diagonalization Algorithms," IEEE Trans. Autom. Control, **32**(2), pp. 115–122.
[39] Willcox, K., and Peraire, J., 2002, "Balanced Model Reduction Via the Proper Orthogonal Decomposition," AIAA J., **40**(11), pp. 2323–2330.
[40] Rowley, C., 2005, "Model Reduction for Fluids, Using Balanced Proper Orthogonal Decomposition," Int. J. Bifurcation Chaos, **15**(3), pp. 997–1013.
[41] Ilak, M., and Rowley, C., 2008, "Modeling of Transitional Channel Flow Using Balanced Proper Orthogonal Decomposition," Phys. Fluids, **20**(3), p. 034103.
[42] Bagheri, S., Henningson, D., Hoepffner, J., and Schmid, P., 2009, "Input-Output Analysis and Control Design Applied to a Linear Model of Spatially Developing Flows," ASME Appl. Mech. Rev., **62**(2), p. 020803.
[43] Barbagallo, A., Sipp, D., and Schmid, P., 2009, "Closed-Loop Control of an Open Cavity Flow Using Reduced-Order Models," J. Fluid Mech., **641**(1), pp. 1–50.
[44] Ahuja, S., and Rowley, C., 2010, "Feedback Control of Unstable Steady States of Flow Past a Flat Plate Using Reduced-Order Estimators," J. Fluid Mech., **645**, pp. 447–478.
[45] Van Dooren, P., Gallivan, K., and Absil, P.-A., 2008, "H_2-Optimal Model Reduction of MIMO Systems," Appl. Math. Lett., **21**(12), pp. 1267–1273.
[46] Gugercin, S., Antoulas, A., and Beattie, C., 2008, "H_2 Model Reduction for Large-Scale Linear Dynamical Systems," SIAM J. Matrix Anal. Appl., **30**(2), pp. 609–638.
[47] Juang, J., and Pappa, R., 1985, "An Eigensystem Realization Algorithm for Modal Parameter Identification and Model Reduction," J. Guid. Control Dyn., **8**(5), pp. 620–627.
[48] Guzmán Iñigo, J., 2015, "Estimation and Control of Noise Amplifier Flows Using Data-Based Approaches," Ph.D. thesis, Ecole Polytechnique, Palaiseau, France.
[49] Van Overschee, P., and De Moor, B., 1996, *Subspace Identification for Linear Systems*, Kluwer Academic Publishers, Dordrecht, the Netherlands.
[50] Guzmán Iñigo, J., Sipp, D., and Schmid, P., 2014, "A Dynamic Observer to Capture and Control Perturbation Energy in Noise Amplifiers," J. Fluid Mech., **758**, pp. 728–753.
[51] Ljung, L., 1999, *System Identification: Theory for the User*, Prentice Hall, Upper Saddle River, NJ.
[52] Ma, Z., Ahuja, S., and Rowley, C., 2011, "Reduced-Order Models for Control of Fluids Using the Eigensystem Realization Algorithm," Theor. Comput. Fluid Dyn., **25**(1–4), pp. 233–247.
[53] Belson, B., Semeraro, O., Rowley, C., and Henningson, D., 2013, "Feedback Control of Instabilities in the Two-Dimensional Blasius Boundary Layer: The Role of Sensors and Actuators," Phys. Fluids, **25**(5), p. 054106.
[54] Huang, S.-C., and Kim, J., 2008, "Control and System Identification of a Separated Flow," Phys. Fluids, **20**(10), p. 101509.
[55] Hervé, A., Sipp, D., Schmid, P., and Samuelides, M., 2012, "A Physics-Based Approach to Flow Control Using System Identification," J. Fluid Mech., **702**, pp. 26–58.
[56] Dovetta, N., Schmid, P., and Sipp, D., 2016, "Uncertainty Propagation in Model Extraction by System Identification and Its Implication for Control Design," J. Fluid Mech., **791**, pp. 214–236.
[57] Juang, J., 1994, *Applied System Identification*, Prentice Hall, Upper Saddle River, NJ.
[58] Brunton, S., Dawson, S., and Rowley, C., 2014, "State-Space Model Identification and Feedback Control of Unsteady Aerodynamic Forces," J. Fluids Struct., **50**, pp. 253–270.
[59] Juillet, F., Schmid, P., and Huerre, P., 2013, "Control of Amplifier Flows Using Subspace Identification Techniques," J. Fluid Mech., **725**, pp. 522–565.
[60] Illingworth, S., Morgans, A., and Rowley, C., 2011, "Feedback Control of Flow Resonances Using Balanced Reduced-Order Models," J. Sound Vib., **330**(8), pp. 1567–1581.
[61] Illingworth, S., Morgans, A., and Rowley, C., 2012, "Feedback Control of Cavity Flow Oscillations Using Simple Linear Models," J. Fluid Mech., **709**, pp. 223–248.
[62] Dahan, J., Morgans, A., and Lardeau, S., 2012, "Feedback Control for Form-Drag Reduction on a Bluff Body With a Blunt Trailing Edge," J. Fluid Mech., **704**, pp. 360–387.
[63] Gelb, A., and Vander-Velde, W., 1968, *Multiple-Input Describing Functions and Nonlinear System Design*, McGraw-Hill, New York.
[64] Ionita, A., and Antoulas, A., 2014, "Data-Driven Parametrized Model Reduction in the Loewner Framework," SIAM J. Sci. Comput., **36**(3), pp. A984–A1007.
[65] Rowley, C., Williams, D., Colonius, T., Murray, R., MacMartin, D., and Fabris, D., 2002, "Model-Based Control of Cavity Oscillations. Part II: System Identification and Analysis," AIAA Paper No. 2002-972.
[66] Rowley, C., Williams, D., Colonius, T., Murray, R., and MacMynowski, D., 2006, "Linear Models for Control of Cavity Flow Oscillations," J. Fluid Mech., **547**, pp. 317–330.
[67] Poussot-Vassal, C., and Sipp, D., 2015, "Parametric Reduced Order Dynamical Model Construction of a Fluid Flow Control Problem," IFAC, **48**(26), pp. 133–138.
[68] Bewley, T., Temam, R., and Ziane, M., 2000, "A General Framework for Robust Control in Fluid Mechanics," Physica D, **138**(3), pp. 360–392.
[69] Bewley, T., Moin, P., and Temam, R., 2001, "DNS-Based Predictive Control of Turbulence: An Optimal Benchmark for Feedback Algorithms," J. Fluid Mech., **447**, pp. 179–225.
[70] Wei, M., and Freund, J., 2006, "A Noise-Controlled Free Shear Flow," J. Fluid Mech., **546**, pp. 123–152.
[71] Cherubini, S., Robinet, J.-C., and De Palma, P., 2013, "Nonlinear Control of Unsteady Finite-Amplitude Perturbations in the Blasius Boundary-Layer Flow," J. Fluid Mech., **737**, pp. 440–465.
[72] Zuccher, S., Luchini, P., and Bottaro, A., 2004, "Algebraic Growth in a Blasius Boundary Layer: Optimal and Robust Control by Mean Suction in the Nonlinear Regime," J. Fluid Mech., **513**, pp. 135–160.
[73] Aubry, N., Holmes, P., Lumley, J., and Stone, E., 1988, "The Dynamics of Coherent Structures in the Wall Region of a Turbulent Boundary Layer," J. Fluid Mech., **192**, pp. 115–173.
[74] Berkooz, G., Holmes, P., and Lumley, J., 1993, "The Proper Orthogonal Decomposition in the Analysis of Turbulent Flows," Ann. Rev. Fluid Mech., **25**(1), pp. 539–575.
[75] Noack, B., Afanasiev, K., Morzynski, M., Tadmor, G., and Thiele, F., 2003, "A Hierarchy of Low-Dimensional Models for the Transient and Post-Transient Cylinder Wake," J. Fluid Mech., **497**, pp. 335–363.
[76] King, R., Seibold, M., Lehmann, O., Noack, B., Morzyński, M., and Tadmor, G., 2005, "Nonlinear Flow Control Based on a Low Dimensional Model of Fluid Flow," *Control and Observer Design for Nonlinear Finite and Infinite Dimensional Systems*, Springer, Berlin, pp. 369–386.
[77] Couplet, M., Basdevant, C., and Sagaut, P., 2005, "Calibrated Reduced-Order POD-Galerkin System for Fluid Flow Modelling," J. Comput. Phys., **207**(1), pp. 192–220.
[78] Bergmann, M., Cordier, L., and Brancher, J., 2005, "Optimal Rotary Control of the Cylinder Wake Using Proper Orthogonal Decomposition Reduced-Order Model," Phys. Fluids, **17**(9), p. 097101.
[79] Bergmann, M., and Cordier, L., 2008, "Optimal Control of the Cylinder Wake in the Laminar Regime by Trust-Region Methods and POD Reduced-Order Models," J. Comput. Phys., **227**(16), pp. 7813–7840.
[80] Bergmann, M., Bruneau, C.-H., and Iollo, A., 2009, "Enablers for Robust POD models," J. Comput. Phys., **228**(2), pp. 516–538.
[81] Gillies, E., 1998, "Low-Dimensional Control of the Circular Cylinder Wake," J. Fluid Mech., **371**(1), pp. 157–178.
[82] Cordier, L., Noack, B., Tissot, G., Lehnasch, G., Delville, J., Balajewicz, M., Daviller, G., and Niven, R., 2013, "Identification Strategies for Model-Based Control," Exp. Fluids, **54**(8), pp. 1–21.
[83] Chaturantabut, S., and Sorensen, D., 2010, "Nonlinear Model Reduction Via Discrete Empirical Interpolation," SIAM J. Sci. Comput., **32**(5), pp. 2737–2764.
[84] Fosas de Pando, M., Schmid, P., and Sipp, D., 2013, "Nonlinear Model-Order Reduction for Oscillator Flows Using POD-DEIM," 66th Annual Meeting of the APS Division of Fluid Dynamics, Pittsburgh, PA, Nov. 24–26, Paper No. M25.00006.
[85] Ştefănescu, R., Sandu, A., and Navon, I., 2015, "POD/DEIM Reduced-Order Strategies for Efficient Four Dimensional Variational Data Assimilation," J. Comput. Phys., **295**, pp. 569–595.
[86] Dandois, J., and Pamart, P., 2013, "NARX Modeling and Extremum-Seeking Control of a Separation," Aerosp. Lab J., **6**, epub.
[87] Burl, J., 1999, *Linear Optimal Control*, Addison-Wesley Longman, Menlo Park, CA.
[88] Cortelezzi, L., Lee, K., Kim, J., and Speyer, J., 1998, "Skin-Friction Drag Reduction Via Robust Reduced-Order Linear Feedback Control," Int. J. Comput. Fluid Dyn., **11**(1–2), pp. 79–92.
[89] Bagheri, S., Brandt, L., and Henningson, D., 2009, "Input–Output Analysis, Model Reduction and Control of the Flat-Plate Boundary Layer," J. Fluid Mech., **620**(1), pp. 263–298.
[90] Barbagallo, A., Dergham, G., Sipp, D., Schmid, P., and Robinet, J.-C., 2012. "Closed-Loop Control of Unsteadiness Over a Rounded Backward-Facing Step," J. Fluid Mech., **703**, pp. 326–362.
[91] Zhao, H., and Bau, H., 2006, "Limitations of Linear Control of Thermal Convection in a Porous Medium," Phys. Fluids, **18**(7), p. 074109.
[92] Horowitz, I., 1993, *Quantitative Feedback Design*. QFT Publications, Boulder, CO.
[93] Vinnicombe, G., 2001. *Uncertainty and Feedback: H_∞ Loop-Shaping and the ν-Gap Metric*, World Scientific, Singapore.
[94] Kook, H., Mongeau, L., and Franchek, M., 2002, "Active Control of Pressure Fluctuations Due to Flow Over Helmholtz Resonators," J. Sound Vib., **255**(1), pp. 61–76.
[95] Doyle, J., 1978, "Guaranteed Margins for LQG Regulators," IEEE Trans. Autom. Control, **23**(4), pp. 756–757.
[96] Zames, G., 1981, "Feedback and Optimal Sensitivity: Model Reference Transformations, Multiplicative Seminorms, and Approximate Inverses," IEEE Trans. Autom. Control, **26**(2), pp. 301–320.
[97] Zhou, K., Doyle, J., and Glover, K., 1996, *Robust and Optimal Control*, Vol. 40, Prentice Hall, Upper Saddle River, NJ.
[98] Apkarian, P., and Noll, D., 2006, "Nonsmooth H_∞ Synthesis," IEEE Trans. Autom. Control, **51**(2), pp. 382.
[99] Petersen, I., and Tempo, R., 2014, "Robust Control of Uncertain Systems: Classical Results and Recent Developments," Automatica, **50**(5), pp. 1315–1335.
[100] Jones, B., Heins, P., Kerrigan, E., Morrison, J., and Sharma, A., 2015, "Modelling for Robust Feedback Control of Fluid Flows," J. Fluid Mech., **769**, pp. 687–722.

[101] Aleksić-Roeßner, K., King, R., Lehmann, O., Tadmor, G., and Morzyński, M., 2014, "On the Need of Nonlinear Control for Efficient Model-Based Wake Stabilization," Theor. Comput. Fluid Dyn., **28**(1), pp. 23–49.
[102] Tachim Medjo, T., 2001, "Robust Control Problems in Fluid Mechanics," Physica D, **149**(4), pp. 278–292.
[103] Hu, C., and Temam, R., 2001, "Robust Boundary Control for the Kuramoto-Sivashinsky Equation," Conference on Optimal Control and Partial Differential Equation, Paris, Dec. 4, 2000, pp. 353–362.
[104] Tachim Medjo, T., and Tcheugoue Tebou, L., 2004, "Adjoint-Based Iterative Method for Robust Control Problems in Fluid Mechanics," SIAM J. Numer. Anal., **42**(1), pp. 302–325.
[105] Tachim Medjo, T., and Tchegoue Tebou, L., 2005, "Robust Control Problems in Fluid Flows," Discrete Control Dyn. Syst., **12**(3), pp. 437–463.
[106] Huerre, P., and Rossi, M., 1998, "Hydrodynamic Instabilities in Open Flows," Collection Alea Saclay Monographs and Texts in Statistical Physics, Cambridge University Press, Cambridge, UK, pp. 81–294.
[107] Schmid, P., 2007, "Nonmodal Stability Theory," Ann. Rev. Fluid Mech., **39**(1), pp. 129–162.
[108] Sipp, D., and Lebedev, A., 2007, "Global Stability of Base and Mean Flows: A General Approach and Its Applications to Cylinder and Open Cavity Flows," J. Fluid Mech., **593**, pp. 333–358.
[109] Blackburn, H., Barkley, D., and Sherwin, S., 2008, "Convective Instability and Transient Growth in Flow Over a Backward-Facing Step," J. Fluid Mech., **603**, pp. 271–304.
[110] Barbagallo, A., Sipp, D., and Schmid, P., 2011, "Input–Output Measures for Model Reduction and Closed-Loop Control: Application to Global Modes," J. Fluid Mech., **685**, pp. 23–53.
[111] Matsumoto, J., and Kawahara, M., 2000, "Stable Shape Identification for Fluid-Structure Interaction Problem Using MINI Element," ASME J. Appl. Mech., **3**, pp. 263–274.
[112] Amestoy, P., Duff, I., L'Excellent, J.-Y., and Koster, J., 2001, "A Fully Asynchronous Multifrontal Solver Using Distributed Dynamic Scheduling," SIAM J. Matrix Anal. Appl., **23**(1), pp. 15–41.
[113] Lehoucq, R., Sorensen, D., and Yang, C., 1998, *ARPACK Users' Guide: Solution of Large-Scale Eigenvalue Problems With Implicitly Restarted Arnoldi Methods*, Vol. 6, SIAM, Philadelphia, PA.
[114] Antoulas, A., 2005, *Approximation of Large-Scale Dynamical Systems*, SIAM, Philadelphia, PA.
[115] Kwakernaak, H., and Sivan, R., 1972, "The Maximally Achievable Accuracy of Linear Optimal Regulators and Linear Optimal Filters," IEEE Trans. Autom. Control, **17**(1), pp. 79–86.
[116] Chen, K., and Rowley, C., 2011, "H_2 Optimal Actuator and Sensor Placement in the Linearised Complex Ginzburg-Landau System," J. Fluid Mech., **681**, pp. 241–260.
[117] Dreyfus, G., Martinez, J.-M., Samuelides, M., Gordon, M., Badran, F., and Thiria, S., 2011, *Apprentissage statistique: Réseaux de neurones-Cartes topologiques-Machines à vecteurs Supports*, Eyrolles, Paris.